REPORT DOCUMENTATION PAGE

Form Approved OMB No. 0704-0188

1. REPORT DATE *(DD-MM-YYYY)*	2. REPORT TYPE	3. DATES COVERED *(From – To)*
15-10-2009	Final Report	26 September 2008 - 26-Sep-09

4. TITLE AND SUBTITLE

DEVELOPMENT OF A NOVEL METHOD FOR THROUGH-WALL IMAGING

5a. CONTRACT NUMBER
FA8655-08-1-3055

5b. GRANT NUMBER

5c. PROGRAM ELEMENT NUMBER

6. AUTHOR(S)

PROFESSOR ROCCO PIERRI

5d. PROJECT NUMBER

5d. TASK NUMBER

5e. WORK UNIT NUMBER

7. PERFORMING ORGANIZATION NAME(S) AND ADDRESS(ES)

SECOND UNIVERSITY OF NAPLES
VIA ROMA 29
AVERSA I 81031
ITALY

8. PERFORMING ORGANIZATION REPORT NUMBER

N/A

9. SPONSORING/MONITORING AGENCY NAME(S) AND ADDRESS(ES)

EOARD
Unit 4515 BOX 14
APO AE 09421

10. SPONSOR/MONITOR'S ACRONYM(S)

11. SPONSOR/MONITOR'S REPORT NUMBER(S)
Grant 08-3055

12. DISTRIBUTION/AVAILABILITY STATEMENT

Approved for public release; distribution is unlimited.

13. SUPPLEMENTARY NOTES

14. ABSTRACT

Through-wall imaging (TWI) consists in imaging objects hidden behind an obstacle by using electromagnetic waves at the microwave frequencies. Developing systems which allow to 'see' through walls gives the ability to detect and localize people, observe room layouts and understand scenarios that are hidden. Accordingly, they can significantly increase the operational effectiveness of many of the organizations that make our society a safer place. The crucial point to be addressed is the presence of the obstacle representing in some cases a wall structure. Indeed, the presence of the wall, on one side, can hinder a successful imaging procedure due the absorption and to the refraction losses it introduces. However, for frequencies ranging from a few hundreds of MHz to 2-3GHz most of the building materials are relatively transparent; which makes high-resolution TWI feasible. On the other side, the presence of the wall has to be embodied in the imaging procedure otherwise blurred images are obtained. In this proposal we aim at developing a novel TWI procedure based on the microwave tomographic approach and to validate it against synthetic and experimental data collected in realistic conditions. Accordingly, the TWI is cast as an inverse scattering problem where the presence of the wall is straightforwardly (with respect to other methods) embodied within the so-called background Green's function. More in detail, despite the inverse scattering problem is non-linear, we adopt a linear reconstruction algorithm based on the Kirchhoff approximation as it allows to meet all the main requirements for a TWI. First of all, it generally allows to determine the scatterers' locations and their geometrical features well beyond the limits of the approximate model. Moreover, it allows to obtain reliable reconstructions free from the local minima problem and is computationally effective, permitting thus to deal with large (in terms of wavelength) investigation domain in almost real time. Finally, well assessed numerical and theoretical tools exist to achieve stability against noise.

15. SUBJECT TERMS

EOARD, Imaging, Tomography, radar

16. SECURITY CLASSIFICATION OF:			17. LIMITATION OF ABSTRACT	18, NUMBER OF PAGES	19a. NAME OF RESPONSIBLE PERSON
a. REPORT	b. ABSTRACT	c. THIS PAGE			A. GAVRIELIDES
UNCLAS	UNCLAS	UNCLAS	UL	68	19b. TELEPHONE NUMBER *(Include area code)* +44 (0)1895 616205

FINAL REPORT
AWARD NO
FA8655-08-1-3055

DEVELOPMENT OF A NOVEL METHOD FOR THROUGH-WALL IMAGING

BY

Raffaele Solimene and Rocco Pierri
Dipartimento di Ingengeria dell'Informazione,
Seconda Università di Napoli,
via Roma 29, Aversa 81031, Italy

AVERSA, 12 OCTOBER 2009

Table of Contents

Table of Contents iv

List of Tables vi

List of Figures vii

Abstract x

Acknowledgements xii

Disclaimer xiii

Disclosure of invention xiv

Introduction 1

1 Methods, Assumptions and Procedures 7
- 1.1 Geometry of the problem and the imaging algorithm 7
- 1.2 Wall parameter estimation procedure 12
- 1.3 Change detection procedure 15

2 Results and Discussion 19
- 2.1 Estimation and reconstruction results obtained by exploiting synthetic data 19
  - 2.1.1 Two-dimensional synthetic results 21
  - 2.1.2 Three-dimensional synthetic results 24
- 2.2 Change detection procedure synthetic results 26
- 2.3 Experimental results 32
  - 2.3.1 2D experimental reconstructions in controlled environment . . 35
  - 2.3.2 In situ 2D experiments 37

2.3.3 3D preliminary reconstructions 41
2.3.4 Testing the change detection procedure by experimental data . 47

3 Conclusions **55**

Bibliography **59**

List of Symbols **66**

List of Abbreviations and Acronyms **68**

List of Tables

2.1 Parameters of the configuration 32

3.1 List of Symbols. 66
3.2 List of Acronyms. 68

List of Figures

1.1 Geometry of the problem. 8

2.1 The case of a concrete wall with two scatterers located far apart from the wall. Actual scatterers are denoted with the dashed white curves. [A]: $1/d(P_{[0,T_e]}\mathcal{F}_\Omega E_{Sav}, P_{[0,T_e]}\mathcal{F}_\Omega E_S^w)$ normalized to its maximum reported as a function of ϵ_b and d. [B]: Tomographic reconstruction obtained by employing the estimated slab parameters. 22

2.2 The case of a concrete wall with two scatterers closely located to the wall. Actual scatterers are denoted with the dashed white curves. [A]: $1/d(P_{[0,T_e]}\mathcal{F}_\Omega E_{Sav}, P_{[0,T_e]}\mathcal{F}_\Omega E_S^w)$ normalized to its maximum reported as a function of ϵ_b and d. [B]: Tomographic reconstruction obtained by employing the estimated slab parameters. 23

2.3 The case of a tuff wall with two scatterers closely located to the wall. Actual scatterers are denoted with the dashed white curves. [A]: $1/d(P_{[0,T_e]}\mathcal{F}_\Omega E_{Sav}, P_{[0,T_e]}\mathcal{F}_\Omega E_S^w)$ normalized to its maximum reported as a function of ϵ_b and d. [B]: Tomographic reconstruction obtained by employing the estimated slab parameters. 24

2.4 The case of a concrete wall with a scatterer in contact to the wall. The actual scatterer's contour is denoted with the dashed white curves. [A]: $1/d(P_{[0,T_e]}\mathcal{F}_\Omega E_{Sav}, P_{[0,T_e]}\mathcal{F}_\Omega E_S^w)$ normalized to its maximum reported as a function of ϵ_b and d. [B]: Tomographic reconstruction obtained by employing the estimated slab parameters. 25

2.5 Layout of the HFSS simulation for the phantom scatterer. 26
2.6 $1/d(P_{[0,T_e]}\mathcal{F}_\Omega E_{Sav}, P_{[0,T_e]}\mathcal{F}_\Omega E_S^w)$ normalized to its maximum reported as a function of ϵ_b and d for the phantom scatterer. 27
2.7 Slice reconstructions of the phantom scatterer. In each slice the phantom's contour is represented by the solid line. 28
2.8 [A]: Isosurface $3D$ reconstruction of a phantom (red surface). [B]: Frontal view (looking at along the z-axis). [C] Lateral view (looking at along the x-axis). 29
2.9 Normalized amplitude reconstruction of the static scatterers. White squares denote actual scatterers. 30
2.10 Normalized TSVD tomographic reconstructions and outcomes of the change detection procedure. [A]: $|\mathcal{R}\gamma_1|$ [B]: $|\mathcal{R}\gamma_1| - |\mathcal{R}\gamma_2|$. [C]: $|\mathcal{R}\gamma_2|$. [D]: $|\mathcal{R}\gamma_2| - |\mathcal{R}\gamma_1|$. [E]: $|\mathcal{R}\gamma_3|$. [F]: $|\mathcal{R}\gamma_3| - |\mathcal{R}\gamma_2|$. White solid lines denote scatterers actually present at the considered instant of time. Dotted lines denote scatterers present at the instant precedent to the considered one. 31
2.11 Picture of the scattering experiment in a semi-anechoic environment. 33
2.12 [A]: Radargram (non-calibrated normalized amplitude Fourier transformed data). [B]: Image obtained by the imaging algorithm. The actual scatterers' cross sections are also depicted as white and red circles. 37
2.13 Picture of the in situ scattering experiment. 38
2.14 [A]: Radargram (non-calibrated normalized amplitude Fourier transformed data). [B]: Pictorial view of the reinforcing grid. 39
2.15 [A]: Picture of the scattering scene. [B]: Reconstruction of a metallic cylinder located at $1m$ beyond the wall. [C]: Reconstruction of a metallic cylinder located at about $2.6m$ beyond the wall. 39
2.16 [A]: Picture of the scattering scene in the case of human scatterers. [B]: Corresponding tomographic reconstruction. 41

2.17 Picture of the planar scanner placed in the anechoic chamber 43
2.18 Picture of the mannequin within the anechoic chamber. 45
2.19 Slice reconstructions of the mannequin. 51
2.20 Frontal view (looking at along the z-axis) of the 3D reconstruction obtained by interpolating the 2D slices. The panel [A] reports the reconstruction only, whereas the panel [B] shows the reconstruction and the mannequin at its actual position. 52
2.21 Frontal view (looking at along the z-axis) of the 3D reconstruction obtained by collecting data according to the NDF. The panel [A] reports the reconstruction only, whereas the panel [B] shows the reconstruction and the mannequin at its actual position. 52
2.22 Normalized TSVD tomographic reconstructions and outcomes of the change detection procedure. [A]: $|\mathcal{R}\gamma_1|$ [B]: $|\mathcal{R}\gamma_1| - |\mathcal{R}\gamma_2|$. [C]: $|\mathcal{R}\gamma_2|$. [D]: $|\mathcal{R}\gamma_2| - |\mathcal{R}\gamma_1|$. 53
2.23 3D reconstructions for two different scatterers layout. The reconstructions and the actual scatterers are both reported. The parameters of the configuration are the same as in Fig. 2.21. The panel [A] is referred as the case 1 and the panel [B] as the case 2. 53
2.24 Difference 3D reconstructions. The reconstructions and the actual scatterers are both reported. The parameters of the configuration are the same as in Fig. 2.21. The panel [A] reports $|\mathcal{R}\gamma_2| - |\mathcal{R}\gamma_1|$ whereas the panel [B] reports $|\mathcal{R}\gamma_1| - |\mathcal{R}\gamma_2|$. 54

Abstract

Through-wall imaging (TWI) consists in imaging objects hidden behind an obstacle by using electromagnetic waves at the microwave frequencies. This problem is of great interest as the aim of detecting and of localizing hidden objects is shared in many applicative contexts, both military and civilian.

For such a problem, the crucial point to be addressed is the presence of the obstacle which can hinder a successful imaging procedure due the absorption and to the refraction losses and which gives rise to blurred images if not properly accounted for. Moreover, in practical situations wall parameters are unknown or at best known with some degree of uncertainty.

Here, the TWI problem is tackled for a three-dimensional geometry where the scatterers are located beyond a wall represented by a dielectric slab whose features are unknown or known with some degree of uncertainty.

In particular, a novel two-step imaging procedure is developed and analyzed.

The first step is concerned with the estimation of the wall thickness and the wall dielectric permittivity. To this end, an estimation procedure which is stable with respect to the noise and to the disturbance introduced by the obscured (i.e., beyond the wall) scatterers has been suitably developed. In particular, the estimation procedure takes into account that the actual measurements concern the total scattered field (i.e., the field reflected by the wall plus the one scattered by the obscured scatterers). This last feature allows us to achieve quick in situ estimations without the need of taking samples of the structure for off line characterization and to overcome the necessity

of identifying wall regions beyond which scatterers are absent. In other words, background measurements (i.e., without the obscured scatterers) become not necessary. This is also of great importance for the imaging stage in that having estimated the wall parameters, the field scattered from the obscured scatterers can be more easily identified within the strong clutter contribution arising from the wall.

As to the imaging stage, the problem is cast as a linear inverse scattering problem and solved by means of a truncated - singular value decomposition (TSVD) based approach. In particular, an imaging procedure based on the microwave tomographic approach is developed. Such a procedure allows us to more straightforwardly and accurately (with respect to other methods present in the literature) account for the wall in the imaging procedure since it enters in the background Green's function definition.

A two-dimensional sliced approach is employed to obtain the three-dimensional scene. Such an imaging method permits to obtain stable high resolution almost real time images.

In this report we present the developed TWI algorithm and give an account of the performances achievable by the proposed TWI method by showing numerical as well as experimental results.

Moreover, a simple strategy to detect changes in a through-the-wall imaging scenarios is presented.

In particular, by exploiting tomographic reconstructions taken at different instants of time it allows us to increase the detectability of scatterers whose positions are varied in two different data collections even though they are embedded within a complex source of clutter background scenario. The feasibility of the technique is demonstrated with both synthetic and experimental data.

The work summarized in this report has led to the publication of three journal papers (see refs. [21, 27, 28]), one conference paper (see ref. [29]) and a further journal paper is now under revision (see ref. [30]).

Acknowledgements

"Effort sponsored by the Air Force Office of Scientific Research, Air Force Material Command, USAF, under grant number FA8655-08-1-3055. The U.S. Government is authorized to reproduce and distribute reprints for Governmental purpose notwithstanding any copyright notation thereon."

Disclaimer

"The grantee is responsible for assuring that every publication of material based on or developed under this project contains the following disclaimer: "The views and conclusions contained herein are those of the author and should not be interpreted as necessarily representing the official policies or endorsements, either expressed or implied, of the Air Force Office of Scientific Research or the U.S. Government."

Disclosure of invention

"We certify that there were no subject inventions to declare during the performance of this grant."

Introduction

Through-wall imaging (TWI) is a research field of increasing interest as the aim of detecting and of localizing hidden objects is shared in many applicative contexts, both military and civilian [1]-[6].

In this framework, the crucial point to be addressed is the presence of the wall.

Indeed, the presence of the wall, on the one hand, can hinder successful imaging due to the absorption and to the refraction losses it introduces. It has been shown that for frequencies ranging from a few hundred MHz to $4-5$ GHz high-resolution TWI is feasible [7]. This is because for such a frequency band most of the building materials are relatively transparent and there is a reasonable tradeoff between wall signal attenuation, achievable spatial resolutions and antennas' sizes [8].

On the other hand, the presence of the wall has to be accounted for in the imaging procedure otherwise blurred images, where scatterers are distorted and shifted form their actual locations, are obtained [9]. This has been done, for example, in [9] where a beamformer relying on an approximate model of the wall (represented by a dielectric slab) has been presented, or in [10], where a synthetic aperture focusing algorithm is adopted with data preliminarily compensated by a factor related to the wall transmissivity matrix.

Here, instead, we adopt a TWI procedure based on a microwave tomographic

approach [11]. Accordingly, the TWI is cast as an inverse scattering problem where the presence of the wall is more straightforwardly (with respect to other methods [9]) and accurately accounted for as it is included within the so-called background Green's function.

Although inverse scattering problems are non-linear [12], we adopt a linear reconstruction algorithm based on the Kirchhoff approximation (as we will consider strong scattering objects) as it allows to meet all the main requirements for a TWI. First of all, it generally allows to determine the scatterers' locations and their geometrical features well beyond the limits of the approximate model [13]. Moreover, it allows to obtain reliable reconstructions free from the local minima problem and it is computationally effective, permitting thus to deal with large (in terms of wavelength) investigation domains in almost real time. Finally, there are well assessed numerical and theoretical tools to achieve stability against noise. In particular, here, the truncated-singular value decomposition (TSVD) of the linearized scattering operator is employed to achieve stable (with respect to uncertainties) reconstructions [14].

In practical situations, the wall parameters are unknown or known with some degree of uncertainty. Wall ambiguities once again result in blurred reconstructions.

To cope with this problem, in [15], a procedure which exploits the measurement array position dependence of the blurring effects was proposed, and subsequently generalized in [16]. Point like scatterers and the canonical case of a single uniform wall represented by a lossless dielectric slab were considered. More in detail, a sequence of reconstructions is performed for different values of the wall parameters varying within an assumed interval for two different measurement array positions. This leads to two different trajectories in the image space which intersect at the actual location of the

scatterers. Hence, either the reconstruction is represented by this intersection or the occurrence of such intersection is adopted to estimate the wall parameters and then the reconstruction is achieved by employing those estimated values.

Afterwards, the same authors proposed an autofocusing procedure based on an iterative scheme where at each step the parameters of the wall are changed according to the optimization of a nonconvex cost functional accounting for the contrast measure of the corresponding reconstructed image and defined in terms of standardized high order moments [17]. The wall and the objects were the same as those already considered in [15] and [16], but in this case the procedure does not require multiple measurement arrays.

In all the previous approaches it is assumed that the data consist of the field scattered by the obscured objects only, while actual measurements concern the total scattered field (i.e., the field reflected by the wall plus the field scattered by the obscured objects). Accordingly, the reliability of the estimation procedures can be negatively affected. This also could occur for all those methods which exploit the late time response of the wall to identify it as in this case multiple reflections within the wall overlap the field scattered by the objects [18, 19].

A simple procedure to *extract* the scattered field from the total field measurements has been proposed in [20]. In that paper a differential strategy is employed to erase from the measurements the field reflected by the wall which is assumed not varying for two consecutive measurement positions. However, even though the clutter due to the wall appears strongly mitigated the knowledge of the wall parameters is still necessary to obtain focussed reconstructions.

To overcome such a drawback we supplement the imaging algorithm with a preliminary estimation procedure which exploits only the early time portion of the total scattered field. As is shown, such a procedure proves to be very accurate and stable with respect to different scatterers' configurations and to the noise [21]. Once the wall parameters are known, clutter can be eliminated by synthetically estimating the field reflected by the wall. Moreover, the imaging algorithm can be suitably developed in order to obtain focused reconstructions.

Most of the contributions in TWI problems deal with two-dimensional ($2D$) configurations (see references previously reported). Achieving a three-dimensional ($3D$) reconstruction of the scene enhances the ability to detect and discriminate targets [21, 22]. However, even under a linear inversion scheme [9, 11], dealing with a 3D geometry could require a high computational cost. Therefore, in order to reduce the computational burden, here we adopt the two-dimensional (2D) sliced approach outlined in [23]. By such an approach it has been shown that, although diffraction and scattering phenomena impair the possibility of obtaining quantitative reconstructions [24], scatterers can be very well localized and their shapes discerned [23].

Generally, the TWI algorithms are concerned with the imaging of stationary targets. Accordingly, information about the geometry of the interior of the building is generally their outcome which is useful, for example, in the design of the rescue operations. In principle, achieving different images of the same scene according to a temporal frame would allow to image time-varying scene offering the possibility of tracking slowly moving objects like humans. This, of course, requires developing an almost real time imaging procedure (measurement acquisition plus signal processing). The imaging algorithms mentioned above take at worst few seconds to achieve

the images, thus the time to acquire the data is a more critical figure. Indeed, the measurements should be taken quasi-instantaneously in order to make negligible the scene's changes during data acquirement otherwise image focusing is deteriorated. To this end, array antennas are a more suitable solution than the more usual sliding antenna (which allows to achieve a multimonostatic or multibistatic configurations) but the necessity to keep the number of the antennas minimum and to account for the global response of the system (mutual coupling between the antennas) have to be satisfied.

A radar system able to track a moving scatterers which exploits array antennas has been demonstrated in [25]. Hence, obtaining a temporal sequence of images of the same spatial region is feasible. Accordingly, this opens the way for solving another crucial question of TWI, that is to discern the human beings from other *static* scatterers present in the scene. By virtue of such results, here we develop a simple procedure to counteract the clutter due to static scatterers present in the scene to be imaged. In particular, the propose procedure is based on the incoherent difference [26, 27] between two tomographic images of the same scene retrieved at different instants of time. It is shown that the procedure is capable to highlight changes in the scene allowing for the detection of a scatterer whose position changes in two different data acquisitions and which would be no easily detectable otherwise.

The performances achievable by the TWI algorithm and by the change detection procedure will be assessed by synthetic and experimental data [28, 29, 30].

The report is organized as follows. In Chapter 1, we describe the geometry of the problem and the adopted configuration. We introduce the formal notation and recall the $2D$ sliced TSVD inversion scheme. Moreover we present the technique

to estimate the wall parameters and the change detection procedure. Chapter 2 is devoted to assess the performances achievable by the estimation procedure, the TWI algorithm and the change detection procedure. To this end, numerical results obtained by adopting synthetic data are reported. In particular, two dimensional examples as well as a $3D$ case for a scatterer resembling the human body are shown. Moreover, we report experimental results for data collected in a laboratory controlled environment and for in situ scattering experiments as well. Conclusions follow.

Chapter 1

Methods, Assumptions and Procedures

In this chapter we describe the geometry and the configuration as well as the mathematical model upon which the inversion algorithm is based. Moreover, we present the TSVD inverse scattering imaging algorithm and the procedure for estimating the wall parameters. Finally, also the change detection strategy is introduced.

1.1 Geometry of the problem and the imaging algorithm

The geometry of the problem is depicted in Fig. 1.1. A target is hidden behind an obstacle represented by a layer having thickness d and dielectric permittivity ϵ_b. The first and the third layers are assumed to be the free-space whose dielectric permittivity is denoted as ϵ_0. The magnetic permeability is everywhere the same as in the free-space μ_0.

The objects are assumed to be $3D$ strong scatterers, that is their electromagnetic

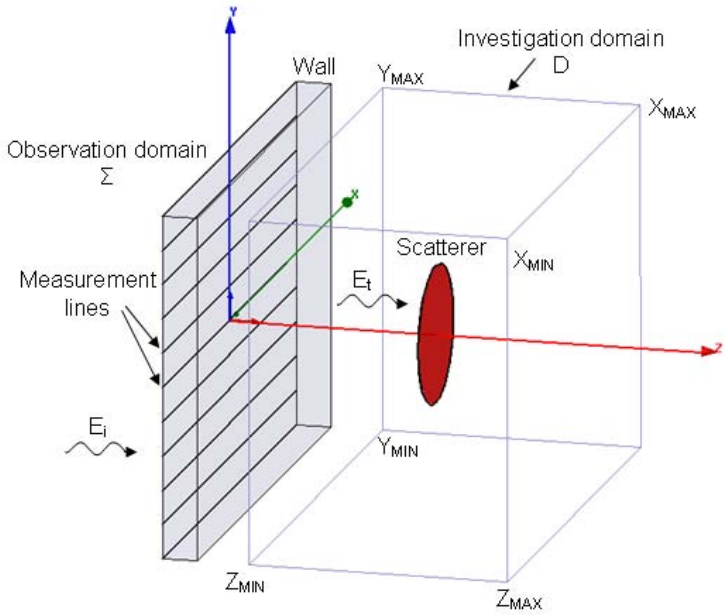

Figure 1.1: Geometry of the problem.

features are very different from those of the free-space, and to reside within a three-dimensional investigation domain D located in the third layer of the background medium (see Fig. 1.1).

The imaging problem consists in retrieving the scatterers'positions and their shapes from scattered field data, observed in a *reflection-mode* configuration over the lines of the domain Σ (see Fig. 1.1), after the scene is interrogated by a known incident field.

To tackle this $3D$ inverse scattering problem, we adopt a two-dimensional sliced approach [23].

First, we consider the illuminating field being provided by a y-polarized $2D$ source

radiating at different frequencies. In particular, the incident field, represented in terms of its plane-wave spectrum $\hat{E}_i(u, k_0)$, is given by

$$\underline{E}_i(x, z, k_0) = \int_{-k_0}^{k_0} \hat{E}_i(u, k_0) \exp\left(-j\sqrt{k_0^2 - u^2}|z - z_S|\right) \exp\left[-ju(x - x_S)\right] du\hat{i}_y, \quad (1.1)$$

k_0 being the wave-number of the free-space ranging within the frequency band $[k_{0min}, k_{0max}]$ and $\underline{r}_S = (x_S, z_S)$ is the source position in the $x - z$ plane. Note that the evanescent part of the plane wave-spectrum has be neglected in (1.1) as it plays a minor role in the scattering process, unless the scatterers are very close to the source.

Moreover, the scattered field collected over each observation line of Σ at different heights y_i (y_i being the i-th component of the height position vector $\underline{y} = (y_1, ..., y_M)$) is exploited to obtain a two-dimensional slice in the $x - z$ plane at the same height. We assume to collect only the y-component of the scattered field. Accordingly, the slice reconstruction is treated as a two-dimensional and scalar inverse problem.

As we are dealing with strong scatterers, we consider the limiting case of metallic scatterers to formulate the problem and linearize the problem by resorting to the Kirchhoff approximation [13]. Accordingly, the mathematical relationship to be inverted to obtain the reconstruction of a slice at height y_i is given by

$$E_S^o(x_m, y_i, k_0) = k_0^2 \int\int_{D_T} G(x_m, x, z, k_0) E_t(x, z, k_0) \times$$

$$\times \gamma(x, y_i, z) dx dz, \quad (1.2)$$

where $E_S^o(\cdot)$ is the field scattered by the objects collected over the segment $-x_M \leq x_m \leq x_M$ at the height y_i of the observation domain Σ and $\gamma(x, y_i, z) = [-\hat{n}(x, y_i, z) \cdot$

$\hat{i}_z]U[-\hat{n}(x,y_i,z)\cdot\hat{i}_z]\delta_{\mathcal{C}}(x,y_i,z)$ is the actual unknown of the 2D problem. $\hat{n}$ and $\hat{i}_z$ are the unitary vectors normal to the scatterers' shape and directed along z, respectively, $U(\cdot)$ is the Heaviside function accounting for the illuminated part of the scatterers, $\delta_{\mathcal{C}}(\cdot)$ is a single-layer distribution supported over the scatterers' contours at the same height as before and $D_T = [-a,a]\times[z_{min},z_{max}]$ denotes the investigation domain cross section (in the $x-z$ plane). Finally, $G(\cdot)$ and $E_t(\cdot)$ are the Green's function relevant for the layered background medium and the field transmitted through the wall and impinging on the scatterers, respectively. In particular, $G(\cdot)$ has the following spectral representation [31]

$$G(x_m,x,z,k_0) = \frac{j}{4\pi}\int_{-\infty}^{\infty}\frac{\tau}{w_0}\exp\left[-jw_0(z-d)\right]\times \exp\left[-jw_0(z_1-z_S)\right]\exp\left[-ju(x_m-x)\right]du, \tag{1.3}$$

where

$$\tau(u,k_0) = \frac{(1-\Gamma_{0b}^2)\exp\left(-jw_bd\right)}{1-\Gamma_{0b}^2\exp\left(-j2w_bd\right)}, \tag{1.4}$$

is the transmission coefficient accounting for the propagation through the slab, $w_i(u,k_0) = \sqrt{k_i^2-u^2}$ with $i\in\{0,b\}$ and

$$\Gamma_{b0}(u,k_0) = \frac{w_0-w_b}{w_0+w_b}, \tag{1.5}$$

is the local reflection coefficient at the air/obstacle interface and where z_1 is the depth of the wall's first interface.

As to $E_t(\cdot)$, by exploiting eqs. (1.4) and (1.1) it can be written as

$$E_t(x,z,k_0) = \int_{-k_0}^{k_0} \tau(u,k_0)\hat{E}_i(u,k_0)\exp\left[-jw_0(z_1-z_S)\right] \times \exp\left[-jw_0(z-d)\right]\exp\left[-ju(x-x_S)\right]du. \quad (1.6)$$

At this point, to obtain $\gamma(\cdot)$ we adopt a reconstruction procedure that we already employed in previous papers (see for examples [13, 23]). First, a regularized solution $\mathcal{R}\gamma(\cdot)$ of eq. (1.2) is obtained by a TSVD inversion scheme [14], that is

$$\mathcal{R}\gamma(x,y_i,z) = \sum_{n=0}^{N_T} \frac{\langle E_S^o(x_m,y_i,k_0), v_n(x_m,k_0)\rangle}{\sigma_n} u_n(x,z), \quad (1.7)$$

with $\{u_n,\sigma_n,v_n\}_{n=0}^{\infty}$ being the singular system of the scattering operator in eq. (1.2), $\langle\cdot,\cdot\rangle$ denotes the scalar product in the data space and N_T is the truncation index. Accordingly, the TSVD achieves regularization by reducing the unknown functional space dimension [14]. Thus, the key question is the choice of truncation index N_T which has to be done by accounting for the noise level, the mathematical features of the operator to be inverted and the available a priori information about the unknown. Different methods exist to select N_T. Such methods can explicitly exploit the knowledge of the noise level (such as the Morozov discrepancy principle) or not (such as the generalized cross validation) [32]. In general, the higher the noise the lower N_T. For the problem at hand, the singular values decay with an exponentially law beyond a certain index. This is shown analytically, for example, for the one-dimensional case in [5] but approximately also holds for the two-dimensional case. Indeed, this reflects the fact that the scattered field has finite number of degrees of freedom (NDF) [33]. Therefore, when the noise is white, it is natural to set the truncation index roughly in correspondence to the index where the singular values start to decay quickly. In the following we will adopt such a criterion.

Having obtained the reconstructions, in order to curtail spurious artifacts due to the noise and to the regularization, a thresholding procedure is adopted [23].

Once the two-dimensional slice reconstructions have been obtained, the three-dimensional representation of the scatterers is achieved by superimposing the two-dimensional reconstructions, that is

$$\mathcal{R}\gamma(x,\underline{y},z) = \begin{pmatrix} \mathcal{R}\gamma(x,y_1,z) \\ ..... \\ \mathcal{R}\gamma(x,y_M,z) \end{pmatrix} \tag{1.8}$$

Finally, the actual $3D$ representation $\mathcal{R}\gamma(x,y,z)$ is obtained by interpolating $\mathcal{R}\gamma(x,\underline{y},z)$ along the y direction.

We remark that in the previous equations, for the sake of simplicity of notation, we have not explicitly indicated the dependence on ϵ_b and d. However, it is clear that the parameters of the wall enter in the definition of the kernel of the operator to be inverted. Moreover, they are necessary to obtain the scattered field data which are given by the difference between the total backscattered field and the background field (the one in absence of the scatterers and due to only the wall structure). Accordingly, when the wall is unknown or known with some degree of uncertainty, the wall has to be estimated prior to achieving imaging. To this end, we adopt the procedure described in next section.

1.2 Wall parameter estimation procedure

A standard way to address the wall estimation problem is to cast it as an optimization problem where a suitable cost functional has to be minimized (or maximized). That is

the dielectric permittivity and the thickness of the wall are estimated as the quantities that globally optimize a functional like

$$(\hat{\epsilon}_b, \hat{d}) = \min_{\epsilon_b, d} \Phi(E_S, \epsilon_b, d). \tag{1.9}$$

As mentioned above, actual measurements generally concern the total scattered field which is given by

$$E_S(x_m, y_i, k_0) = E_S^w(x_m, y_i, k_0) + E_S^o(x_m, y_i, k_0), \tag{1.10}$$

where E_S^o is the field scattered by the objects as given in eq. (1.2) (a part from multiple reflections between the wall and the objects) and E_S^w is the field reflected by only the wall which, in turn, is given by

$$E_S^w(x_m, y_i, k_0) = \int_{-k_0}^{k_0} \Gamma(u, k_0) \hat{E}_i(u, k_0) \exp(-2jhw_0) du, \tag{1.11}$$

where a monostatic configuration (i.e., with the source and the receive positions coinciding.) is cosidered, $h = z_1 - z_S$ is the distance of the source from the front side of the wall and $\Gamma(\cdot)$ is the slab reflection coefficient

$$\Gamma(u, k_0) = \frac{\Gamma_{0b} - \Gamma_{0b} \exp(-j2w_b d)}{1 - \Gamma_{b0}^2 \exp(-j2w_b d)}. \tag{1.12}$$

The estimation methods listed in the introduction do not take into account eq. (1.10) and this could affects negatively their reliability. To overcome such a problem we estimate the slab parameters by minimizing the following cost functional

$$(\hat{\epsilon}_b, \hat{d}) = \min_{\epsilon_b, d} \tilde{d}(P_{[0,T_e]} \mathcal{F}_\Omega E_{Sav}, P_{[0,T_e]} \mathcal{F}_\Omega E_S^w), \tag{1.13}$$

where $\tilde{d}(\cdot,\cdot)$ is a distance functional, $\mathcal{F}_\Omega$ is the Fourier transform operator with respect to the angular frequency ω supported over the available frequency band $\Omega = [ck_{0min}, ck_{0max}]$, $P_{[0,T_e]}$ is the time limiting projector over the interval $[0, T_e]$, with $T_e = 2(\sqrt{\epsilon_b}d/c + h)$, c being the speed of light in the free space. Finally, E_{Sav} is E_S averaged over all the measurements taken at the different y_i.

In other words, the parameters of the wall are estimated by minimizing the mismatch between the measured total scattered field and the model slab field by accounting for only their early time portion. In particular, T_e is chosen so that the contributions to E_S arising from the scattering objects located beyond the slab are mainly concentrated outside such an interval and thus play a minor role in the estimation procedure.

Note that even though eq. (1.13) measures the mismatch between data and model in time domain, data are collected and the inversion scheme works in the frequency domain. Therefore, time domain is introduced only to give a physically useful interpretation of the mathematical range of the linear operator $P_{[0,T_e]}\mathcal{F}_\Omega$ involved in eq. (1.13).

It is worth remarking that the estimation procedure in eq. (1.13) is similar to the one presented in [10] but some differences have to be pointed out. First, in [10] the total field is Fourier transformed, time gated and then Fourier transformed once again so that the minimization is achieved in the frequency domain. Conversely, this last step is not required for the estimation procedure herein proposed. Moreover, while in [10] the estimation exploits the measurements taken at a single position of the receiving antenna, in the method developed here the averaged E_S is adopted. By doing so, it is expected that the proposed estimation procedure improves its

robustness against the disturbances due to the obscured scatterers and to the noise. Finally, in the estimation procedure of eq. (1.13) a varying time gating interval T_e, which depends on the trial values of ϵ_b and d, is adopted and automatically updated while the minimization proceeds. This avoids the need of a preliminary look at the time domain traces.

Some comments to relate the proposed method to the ones reported in [15, 16, 17] are in order. All these methods cast the estimation problem as in eq. (1.9). However, while in eq. (1.13) the optimization stage is achieved in the data space, in [15, 16, 17] it is performed in the image space. Therefore, as the proposed method does not require to achieve reconstructions it is expected to be faster in estimating the wall. Furthermore, approaches reported in [15, 16, 17] have been studied for point-like scatterers whereas no assumption about the scatterers is done in the proposed estimation procedure.

Finally, our method as well as the ones reported in [15, 16, 17] consider a homogeneous slab as wall. However, in many realistic situations such a hypothesis does not hold (for example in the case of a multi-layered wall) and the number of parameters necessary to describe the wall (and to be searched for from the estimation procedure) increases affecting the effectiveness of the optimization stage.

1.3 Change detection procedure

In a typical TWI problem the scene to be imaged is rather complex in the sense that it can contain several scatterers of different nature. Therefore, to discern, for example, human beings from other scatterers is generally a very hard task by exploiting an imaging procedure only.

Accordingly, in this section, we address the problem of improving the detectability of a target against the clutter due to static scatterers present within the investigation domain D.

The target of interest is assumed slowly moving in the sense that it is at rest while the aperture is synthesized but its position can change in two different measurement surveys. Of course, how quick the scatterer can move depend on the time required for data collection and hence on the adopted radar system [25]. The scattered field E_S^o arising from the objects located beyond the wall of Eq. (1.2) can be then decomposed as

$$E_S^o(x_m, y_i, k_0) = E_{SC}(x_m, y_i, k_0) + E_{ST}(x_m, y_i, k_0), \tag{1.14}$$

where $E_{SC}(x_m, y_i, k_0)$ denotes the clutter contribution and $E_{ST}(x_m, y_i, k_0)$ is the field due to the object of interest. Consequently, clutter removal can be cast as the problem of filtering out $E_{SC}(x_m, y_i, k_0)$ from $E_S^o(x_m, y_i, k_0)$.

To this end, a filter can be properly designed and tuned on the clutter properties with the constraint of preserving as much as possible $E_{ST}(x_m, y_i, k_0)$ which is needed for imaging purposes.

In conventional radar systems the so-called moving target indicator (MTI) techniques are designed to detect moving targets against a strong stationary clutter. This is possible because of clutter and targets have different Doppler spectra. Accordingly, a Doppler filtering is designed to cancel the zero Doppler spectral content [34]. A similar filtering is exploited in ground penetrating radar (GPR) imaging [35] where a high-pass filtering suppresses the low harmonic spatial content in order to mitigate the clutter arising from the air/soil interface. Unfortunately, for the case of concern

herein, neither the frequency Doppler shift (as in MTI) nor the difference in the spatial spectral content can be exploited. Indeed, all the scatterers are assumed to be at rest during data acquirement. Moreover, they have all a finite spatial support hence filtering the spatial spectrum as in [35] is not useful.

However, if we could take N different data surveys, that is

$$E_S^o(x_m, y_i, k_0, m) \qquad m \in (1, 2, ..., N), \tag{1.15}$$

a similar filtering as in [35] could be applied if data are Fourier transformed with respect to the discrete variable m.

Here, we adopt a different procedure where the change detection is achieved by means of the difference between two different tomographic reconstructions of the same spatial region.

Removing clutter by means of a difference procedure has been already documented in the literature. In [26] and [36], the coherent and incoherent difference between two images is exploited, respectively.

However, in both papers one of the two images refers to the case where the scatterer of interest is not present. This substantially corresponds to exploiting the background measurement which is difficult to obtain in practical TWI scenarios.

In order to relax the need of the reference image (or, equivalently, reference data), here the following procedure is exploited.

Say $\mathcal{R}\gamma_m(x, y_i, z)$ the tomographic reconstruction obtained by processing the data collected at the m-th instant. Then, we consider

$$|\mathcal{R}\gamma_m(x, y_i, z)| - |\mathcal{R}\gamma_{m-1}(x, y_i, z)| \tag{1.16}$$

as the *difference* image at the m-th instant of time, with $|\cdot|$ being the modulus of its argument. In other words, the reconstruction at the m-th instant of time is obtained by subtracting pixel by pixel the modulus of the tomographic reconstructions obtained by exploiting $E_S^o(x_m, y_i, k_0, m)$ and $E_S^o(x_m, y_i, k_0, m-1)$, respectively.

The resulting *difference* image is then positively thresholded. This allows to image the targets at the position it was occupying while the m-th survey was being performed. In fact, the difference sign in eq. (1.16) will roughly cancel the reconstruction of static scatterers whereas the reconstruction of the target at time $m-1$ will appear under the negative sign and it is then erased by the positive threshold.

This explains why we chose to achieve clutter mitigation in the image domain rather than in data domain. In fact, by inverting $E_S^o(x_m, y_i, k_0, m) - E_S^o(x_m, y_i, k_0, m-1) = E_{ST}(x_m, y_i, k_0, m) - E_{ST}(x_m, y_i, k_0, m-1)$ (which would correspond to the coherent difference in the image domain) would allow, in principle, a better clutter cancelation (in fact due to the nonlinearity of the modulus function the reconstruction of static scatterers is in general different for each measurement survey as they do not sum incoherently to the ones of the targets) but we would be not able to discern the actual target position. This last circumstance occurs, for example, in the work presented in [37] where the coherent subtraction, applied to the data, was exploited for two different time acquisitions at a fixed position. However, there the aim was to remove the wall clutter.

Of course, if the target does not change its position during two different surveys the proposed procedure will fail because also the target itself will be erased in the *difference* reconstruction.

Chapter 2

Results and Discussion

In this chapter we assess the effectiveness of the procedures discussed previously. In particular, we will be mainly concerned with numerical examples but also some experimental results, in a laboratory controlled environment as well as for in situ cases, are presented.

2.1 Estimation and reconstruction results obtained by exploiting synthetic data

In this section we start to assess the performances achievable by the estimation procedure and by the tomographic TWI approach by adopting synthetic data.

In particular, in the following, the distance $\tilde{d}(a, b)$ in eq. (1.13) is chosen as the usual square Euclidean norm $\|a - b\|^2$.

For all the reconstruction results reported in this section, the measurement and the scattering configurations are characterized as follows. An investigation domain $D = [-1, 1] \times [-1, 1] \times [0.4, 3]m^3$ is considered whereas the incident field consists of plane waves impinging along the z-axis and varying frequency within the band of

$[0.3, 1]GHz$. In particular, a frequency step of $35MHz$ (which means 21 different frequencies) is chosen accordingly to the results reported in [38] where the frequency step to avoid data redundancy is derived in terms of the extent along the depth (i.e., along the z-axis) of the investigation domain.

A measurement aperture $\Sigma = [-1, 1] \times [-1, 1]m^2$ is considered. More in detail, 11 slices at different evenly spaced heights, within the interval $[-1, 1]m$ along the y-axis, are taken and for each slice the scattered field is collected at 11 evenly spaced points over the segment $[-x_M, x_M] = [-1, 1]m$ of the x-axis. In particular, the number of observation points for each slice is chosen according to the *degrees of freedom* of the scattered field for a two-dimensional object of a size equal to D_T in correspondence to the highest adopted frequency [33].

Such an estimation refers to free-space configurations but still holds for the configuration at hand. This can be deduced by the study about the spatial spectral filtering introduced by the scattering operator for a three-layered background medium reported in [11]. All the observation points are characterized by $z = 0$ within the specified reference frame (see Fig. 1.1).

In order to test the reconstruction algorithm against noisy data, the total scattered field E_S is corrupted by an independent noise. In particular, two independent zero-mean white Gaussian noise processes are added to the real and imaginary part of the data so as to obtain a very low (in the framework of inverse scattering problems) signal-to-noise ratio (SNR) of 5 dB in all the cases.

As only a qualitative reconstruction of the geometrical features of the targets can be obtained, according to the arguments reported in [13], in all the following figures the normalized real part of the reconstructions is displayed. All the reconstructions

are obtained by retaining in the singular value expansion (1.7) the singular functions corresponding to the singular values not below $20dB$ of the maximum singular value. Furthermore, each slice is thresholded at the same value as described in [23] (see also reference [18] therein reported for more details).

We start by showing results concerning two-dimensional slices. Then, a three-dimensional case, with the scatterer being a phantom resembling the human body, is considered.

2.1.1 Two-dimensional synthetic results

In this section we test the imaging algorithm against synthetic data for two-dimensional cases.

For all the two-dimensional example reported below, the total scattered field E_S^o has been computed by means of the method of moments (MOM) whereas the current induced over the scatterers has been determined by adopting the electric field integral equation (EFIE) [39].

The first reconstruction example is shown in Fig. 2.1. It concerns a slab with $\epsilon_b = 9\epsilon_0$ and $d = 0.2$ m, representative of a concrete masonry structure [17, 40], with two metallic cylinders of elliptical cross section, miming the cross section of a human body, located beyond it so that their centers are at $1.8m$ and $2m$ from the wall (see dashed white curve of panels [B] to see the scatterers' positions). In Fig. 2.1 (panel [A]) $1/d(P_{[0,T_e]}\mathcal{F}_\Omega E_{Sav}, P_{[0,T_e]}\mathcal{F}_\Omega E_S^w)$ normalized to its maximum is depicted. It is computed by adopting the total scattered field averaged over the 11 acquisitions of one single measurement line while the slab parameters vary within the bounded domain $[2, 11] \times [0.1, 0.4]m$ of the $\epsilon_b/\epsilon_0 - d$ plane. A step of 0.1 along ϵ_b/ϵ_0 and of

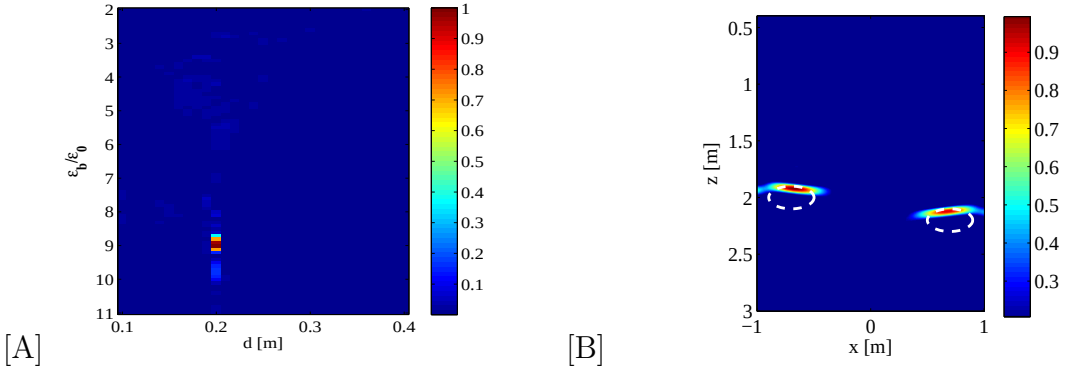

Figure 2.1: The case of a concrete wall with two scatterers located far apart from the wall. Actual scatterers are denoted with the dashed white curves. [A]: $1/d(P_{[0,T_e]}\mathcal{F}_\Omega E_{Sav}, P_{[0,T_e]}\mathcal{F}_\Omega E_S^w)$ normalized to its maximum reported as a function of ϵ_b and d. [B]: Tomographic reconstruction obtained by employing the estimated slab parameters.

$1cm$ in d is adopted (such a discretization is maintained for all the examples).

As can be seen, the estimator peaks around the slab's true parameters achieving the maximum for the actual slab parameters. The corresponding reconstruction is shown in the same figure (panel [B]) where the scatterers are detected and correctly localized.

We outline that, as only two parameters have to determined, building up the estimator for the whole ambiguity set is achieved in almost real time on a standard laptop computer. Accordingly, for the cases at hand it is not necessary to exploit an optimization algorithm (as in [17]) which can be trapped in a local extreme of the cost functional.

For the same measurement configuration and background scenario as in Fig. 2.1 we now consider the case where the two scatterers are more closely located to the wall (their centers are now at $0.5m$ and $0.7m$ from the wall). For such a situation, the

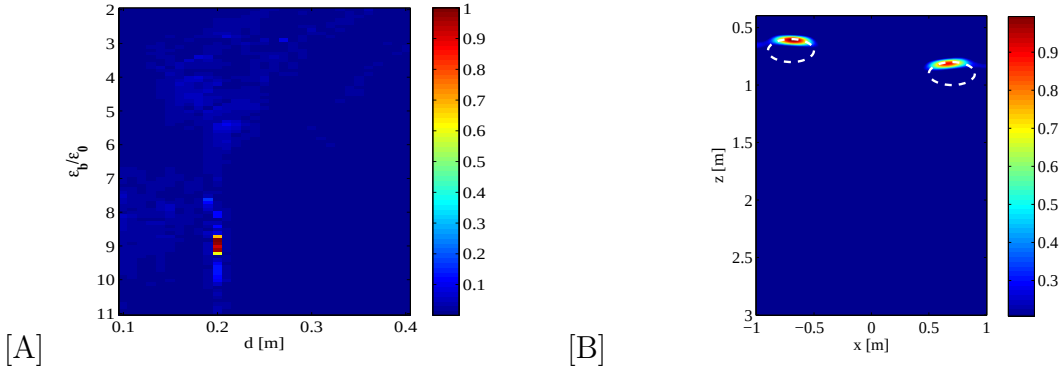

Figure 2.2: The case of a concrete wall with two scatterers closely located to the wall. Actual scatterers are denoted with the dashed white curves. [A]: $1/d(P_{[0,T_e]}\mathcal{F}_\Omega E_{Sav}, P_{[0,T_e]}\mathcal{F}_\Omega E_S^w)$ normalized to its maximum reported as a function of ϵ_b and d. [B]: Tomographic reconstruction obtained by employing the estimated slab parameters.

"disturbance" introduced by the objects on the wall estimation procedure increases. Nevertheless, as can be see from Fig. 2.2, the estimation procedure works as well as in the previous case. Indeed, the estimator achieves the maximum at $\hat{\epsilon}_b = 8.8\epsilon_0$ and $\hat{d} = 0.2$, that are very close to the actual parameters, and once again the objects are detected and precisely localized.

As a second example, we consider a slab with $\epsilon_b = 4\epsilon_0$ and $d = 0.2$ m. Such parameters are representative of a tuff masonry structure which is typical of Campania region old buildings in the south of Italy. The corresponding reconstructions are reported in Fig. 2.3 where the same configuration as already addressed in Fig. 2.2 is considered. Also in this case the estimation procedure practically yields the actual wall parameters and the scatterers are precisely localized.

Indeed, the procedure proves to work well also for scatterers very close to the wall. To demonstrate this, we report Fig 2.4 which refers to the same wall parameters as

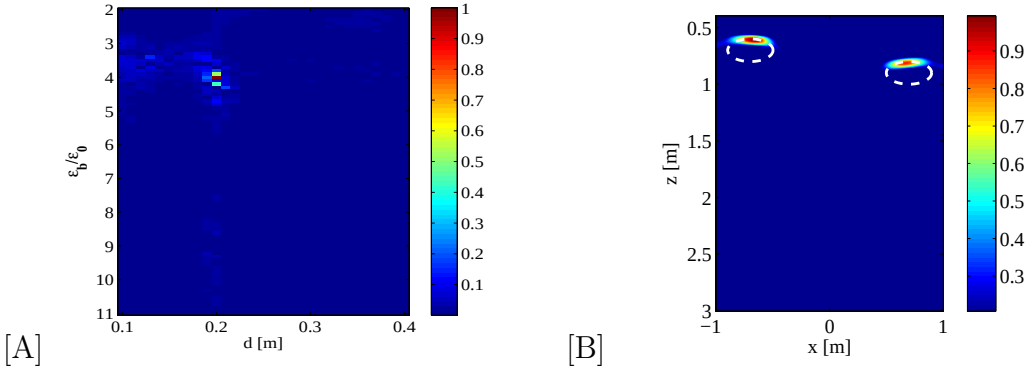

Figure 2.3: The case of a tuff wall with two scatterers closely located to the wall. Actual scatterers are denoted with the dashed white curves. [A]: $1/d(P_{[0,T_e]}\mathcal{F}_\Omega E_{Sav}, P_{[0,T_e]}\mathcal{F}_\Omega E_S^w)$ normalized to its maximum reported as a function of ϵ_b and d. [B]: Tomographic reconstruction obtained by employing the estimated slab parameters.

for Fig. 2.1 and to a scattering object whose contour is in contact with the wall.

2.1.2 Three-dimensional synthetic results

Here, we turn to consider the three-dimensional more realistic TWI problem depicted in Fig. 2.5.

In particular, we consider the reconstruction of a scatterer resembling the human body. To this end, a homogeneous anthropomorphic phantom of $1.80m$ in height, has been considered. Its dielectric permittivity and conductivity are $\epsilon = 20\epsilon_0$ and $\sigma = 0.5S/m$, respectively. Such a scatterer is located about $0.9m$ beyond a finite tuff wall which is $3m$ width, $2.5m$ height and $0.2m$ thick. For this example, the synthetic data have been obtained by exploiting the commercial HFSS tool which is a full 3D FEM based code [41] and once again plane wave illumination is considered. The layout of the HFSS simulation is shown in Fig. 2.5.

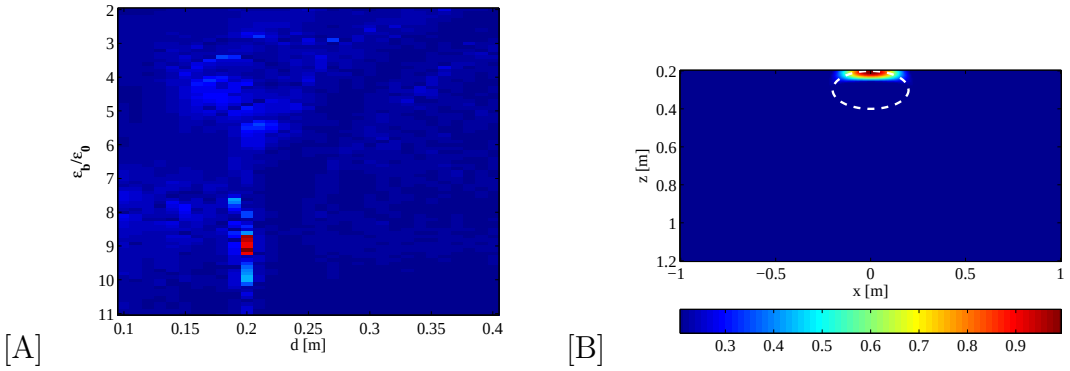

Figure 2.4: The case of a concrete wall with a scatterer in contact to the wall. The actual scatterer's contour is denoted with the dashed white curves. [A]: $1/d(P_{[0,T_e]}\mathcal{F}_\Omega E_{Sav}, P_{[0,T_e]}\mathcal{F}_\Omega E_S^w)$ normalized to its maximum reported as a function of ϵ_b and d. [B]: Tomographic reconstruction obtained by employing the estimated slab parameters.

Note that, owing to the transversal finiteness of the wall, further problems in the estimation procedure could arise. This is because not only the field scattered from the obscured objects but also the one arising from the transversal edges of the wall will perturb the model field E_S^w which accounts for a slab not limited transversally.

In this case the cost functional is obtained by averaging the total scattered field E_S over all the 121 acquisitions and its behavior is reported in Fig. 2.6. The functional is once again peaked around the actual wall parameters. In particular, it achieves the maximum for $\hat{\epsilon}_b = 3.9\epsilon_0$ and $\hat{d} = 0.2$ m. Such parameters are employed to evaluate the Green's function and E_S^w, according to eqs. (1.3) and (1.11), respectively. The slab field is then subtracted to the computed E_S to obtain E_S^o. The latter is then provided to the reconstruction algorithm whose outcome is reported in Figs. 2.7 and 2.8. In Fig. 2.7, 9 of the 11 computed slices are reported. As can be seen, in each slice the scatterer is successfully localized. However, the arms and the legs are not

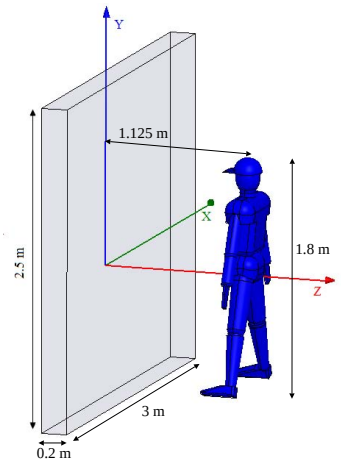

Figure 2.5: Layout of the HFSS simulation for the phantom scatterer.

discernable. Notwithstanding, in the corresponding $3D$ reconstruction (Fig. 2.8) the phantom is very well localized (as obvious from the slices) and its silhouette roughly retrieved, hence it greatly improve the understanding about the scatterer.

2.2 Change detection procedure synthetic results

In this section we show some synthetic examples to check the effectiveness of the proposed change detection procedure.

The following synthetic examples refer to a $2D$ geometry for a multimonostatic configuration (i.e., the receiving antenna is located at the same position as the source while the latter moves to synthesize the measurement aperture). A filamentary current ($2D$ dipole) provides the incident field. The reconstructions have been obtained for a scattering configuration whose parameters are reported in Tab. 2.1.

The data are synthesized in time domain thanks to the free code GPRMAX based

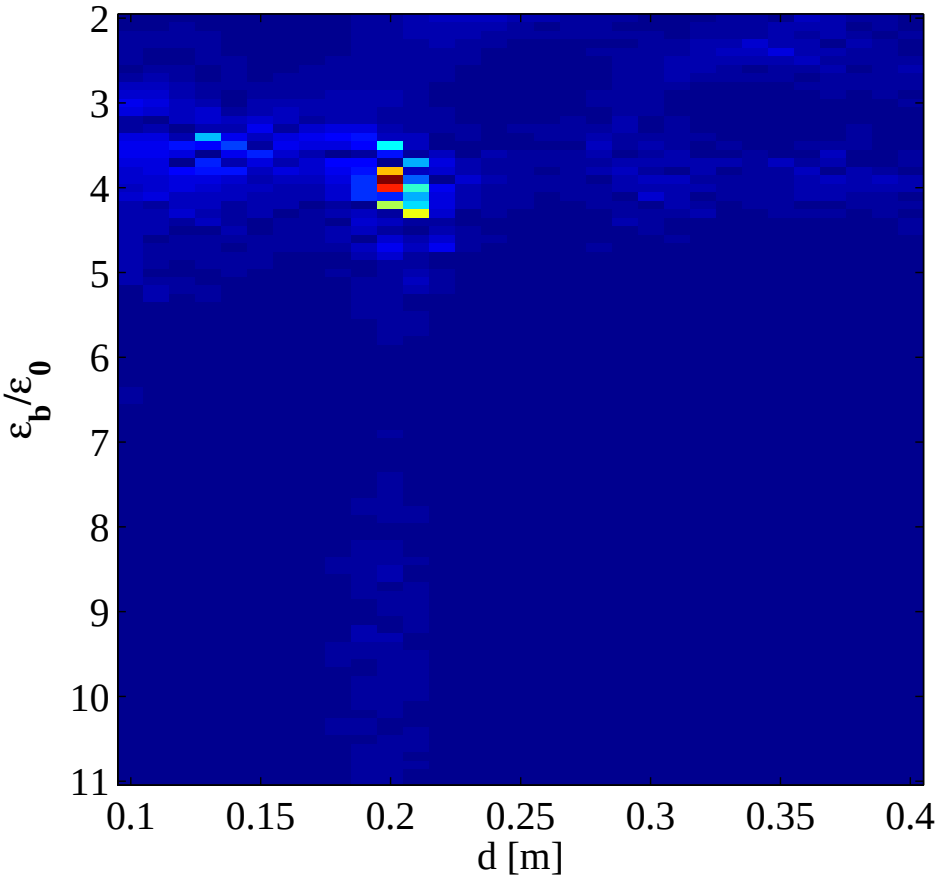

Figure 2.6: $1/d(P_{[0,T_e]}\mathcal{F}_\Omega E_{Sav}, P_{[0,T_e]}\mathcal{F}_\Omega E_S^w)$ normalized to its maximum reported as a function of ϵ_b and d for the phantom scatterer.

on a FDTD method [42] and then Fourier transformed in the frequency domain. Finally, the reconstructions are obtained according to eq. (1.7) where the singular values above 0.2 times the maximum one are retained.

The clutter scenario consists of two square scatterers having side equal to $0.2m$ whose centers are at $(-0.4, 0.9)m$ and $(0.3, 1.1)m$, respectively. The shallower square has a dielectric permittivity of $4\epsilon_0$ whereas the other one of $9\epsilon_0$.

The corresponding reconstruction (along with to the scatterers layout) is reported

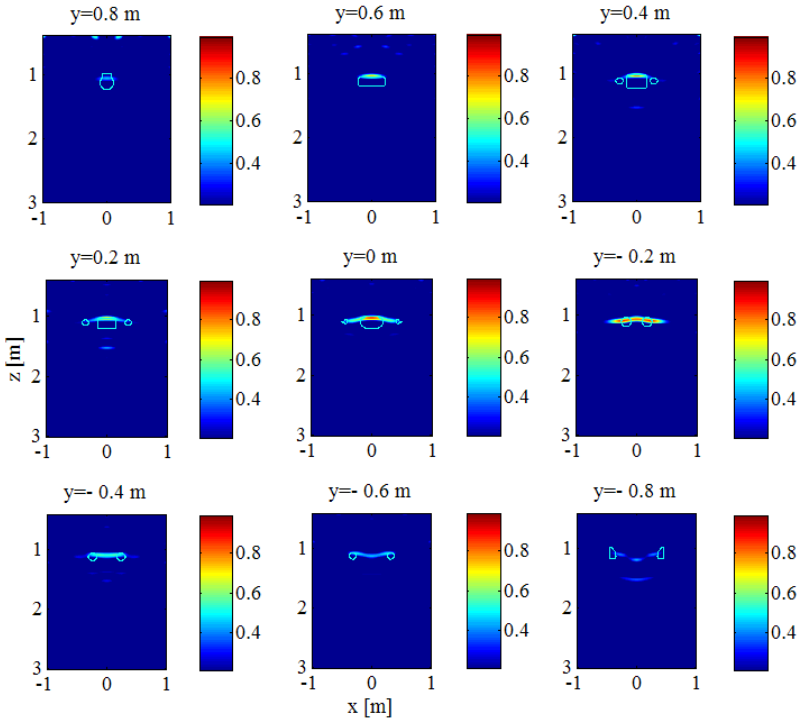

Figure 2.7: Slice reconstructions of the phantom scatterer. In each slice the phantom's contour is represented by the solid line.

in Fig.2.9. As can be seen, both the upper and lower edges of the objects are clearly detected and localized. However, as the electromagnetic velocity within the square objects are different from the one assumed in the linear model, the lower edges are not in their actual positions but are delocalized as they appear more deeply located.

Now, as a target to be detected within the above depicted scenario, we consider a circular object of radius equal to $0.1m$ and dielectric permittivity $20\epsilon_0$. During each single data collection the target is at rest whereas its position can change in two different data collections.

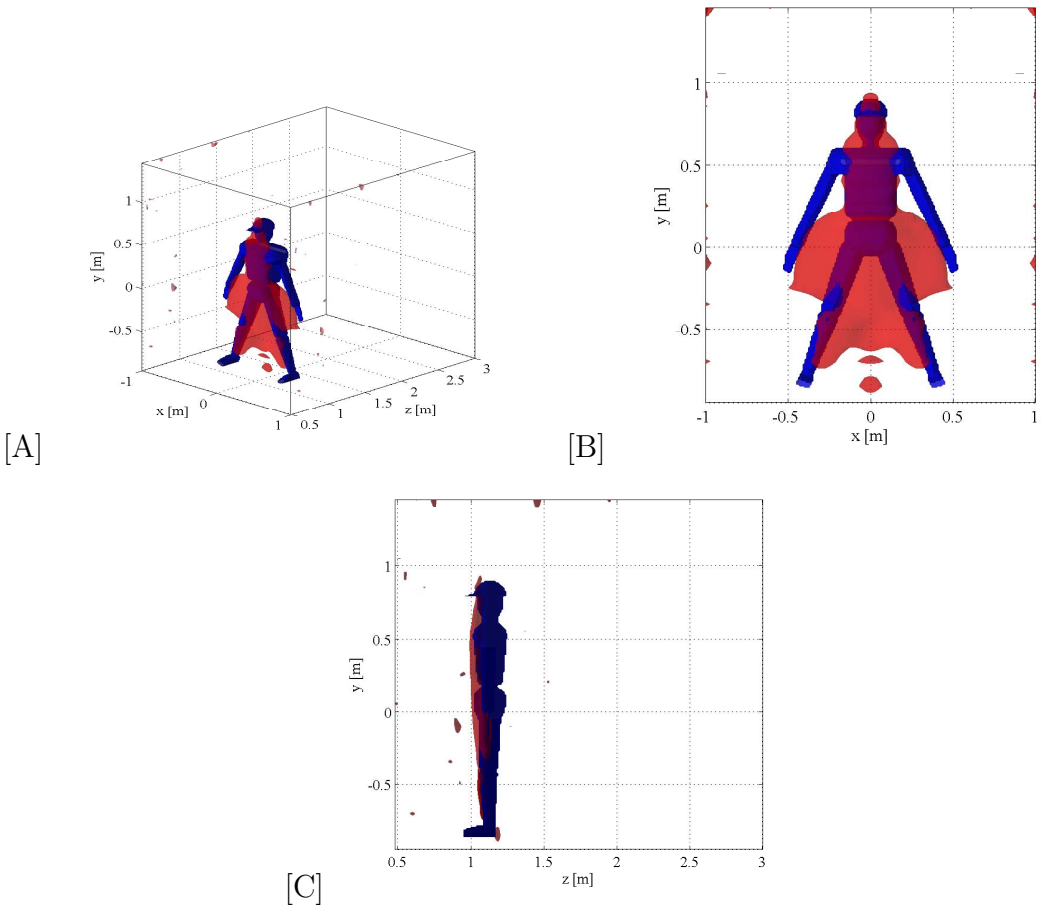

Figure 2.8: [A]: Isosurface $3D$ reconstruction of a phantom (red surface). [B]: Frontal view (looking at along the z-axis). [C] Lateral view (looking at along the x-axis).

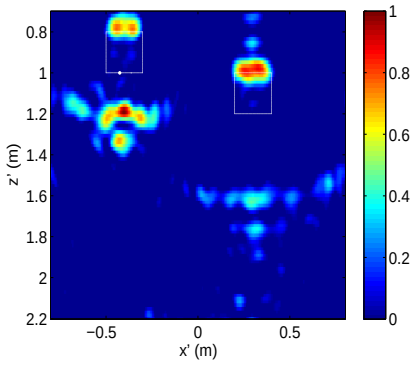

Figure 2.9: Normalized amplitude reconstruction of the static scatterers. White squares denote actual scatterers.

In particular, we consider the following situations:

$m = 1$, the target center is at $(0, 1.9)m$

$m = 2$ the target center is at $(0.3, 1.6)m$

$m = 3$, the target center is at $(0, 1.3)m$.

The tomographic reconstructions for such scatterer configurations and the corresponding results obtained by the *difference* procedure are reported in Fig. 2.10.

By comparing panels $[A]$ and $[B]$ and panels $[C]$ and $[D]$ of Fig. 2.10 it is evident that the proposed procedure allows to increase the detectability of the circular scatterer. Of particular interest is the case reported in panel $[D]$ where the change detection procedure allows to discern the target which is overwhelmed by the reconstruction of deeper side the square object in front of it (see panel $[C]$). In panel $[D]$ the circular target is already well visible. However, the change detection procedure allows to better identify the scatter against the artifacts due to the square objects.

Analogues results (here not reported) have been also obtained for the more complex background scenario resembling the room of a building addressed in [43].

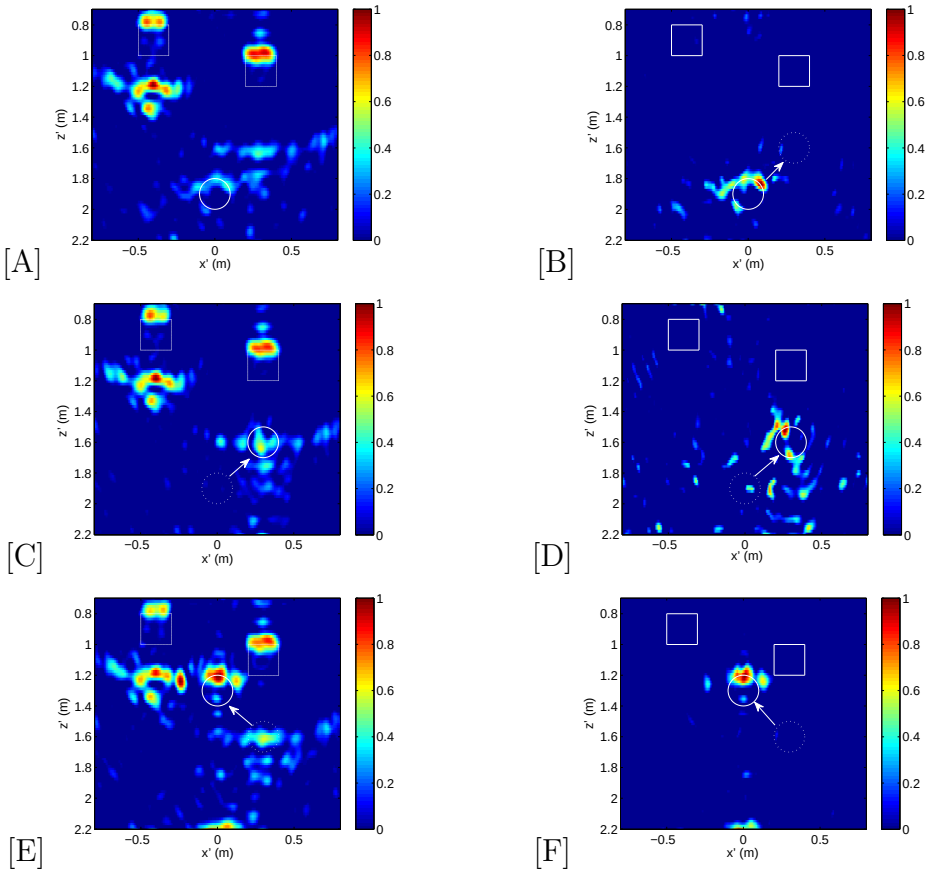

Figure 2.10: Normalized TSVD tomographic reconstructions and outcomes of the change detection procedure. [A]: $|\mathcal{R}\gamma_1|$ [B]: $|\mathcal{R}\gamma_1| - |\mathcal{R}\gamma_2|$. [C]: $|\mathcal{R}\gamma_2|$. [D]: $|\mathcal{R}\gamma_2| - |\mathcal{R}\gamma_1|$. [E]: $|\mathcal{R}\gamma_3|$. [F]: $|\mathcal{R}\gamma_3| - |\mathcal{R}\gamma_2|$. White solid lines denote scatterers actually present at the considered instant of time. Dotted lines denote scatterers present at the instant precedent to the considered one.

Table 2.1: Parameters of the configuration

Wall dielectric permittivity ϵ_b	$4\epsilon_0$
Wall conductivity σ_b	$0.05 S/m$
Wall thickness d	$0.24m$
Investigation domain D_T	$[-0.8, 0.8] \times [0.7, 2.2] m^2$
Σ	$[-0.8, 0.8] m$
Spatial step of measurements	$0.04m$
Frequency band	$[1, 2.5] GHz$
Frequency step	$50 MHz$
Offset TX-RX	0m

2.3 Experimental results

This section is devoted to showing some experimental reconstructions in order to assess the reconstruction capabilities of the inversion algorithm. In particular, the experimental results refer for a scattering scenario located within a laboratory controlled environment (i.e., the Electromagnetic Diagnostic Laboratory at the Second University of Naples) and also for in situ experiments.

The imaging problem for realistic situations is intrinsically a three-dimensional problem. However, accordingly to the discussion reported in the previous chapter, we perform the reconstructions according to the sliced approach by assuming to deal with a two-dimensional and scalar problem.

To collect data we used a portable continuous wave stepped frequency radar system (see Fig. 2.11) developed and implemented under a cooperation between the Second University of Naples and Ingegneria dei Sistemi [44]. The main components of such a system are the electronic unit, the automatic positioning system and the antennas. The data acquisition procedure is supervised by a laptop via a USB port

thanks to a customized software written in Labview language. In particular, the software permits to choose the number and the step of the frequency, the radiated power and the number and spacing of the spatial measurement as well as the kind of acquisition.

Figure 2.11: Picture of the scattering experiment in a semi-anechoic environment.

The electronic unit is made up of a transmitter and two receiving channels which can work in the frequency $800MHz-4GHz$ band. The maximum number of frequencies that can be taken is 3200 hence a minimum frequency step of $1MHz$ is allowed. Each single frequency measurement requires roughly $1ms$. The I and Q components of the signal are acquired. The maximum transmitter power is $0dBm$. The electronic

unit permits to control three antennas, one transmitting and two receiving. The antennas are automatically positioned thanks to a slide driven by a stepped motor. The slide is $2.5m$ long and allows a measurement line of $2m$ at most. The offset between the antennas is fixed but it can be adjusted manually at any desired value between $10cm$ and $1m$.

In the following experiment we used only two antennas, two rectangular ridged horns (Schwarzbeck mod. BBHA9120A) which can work between $800MHz$ and $5GHz$, linearly polarized along the y-axis.

A more detailed description of the hardware system can be found in [44].

Before proceeding to the reconstructions, the radar system must be calibrated to remove the systematic errors due to the radar circuitry, the cables, the cable-antenna transitions and to the antennas. Indeed, from the actual measurements concerning the scattering parameter S_{21} the scattered field has to be obtained.

As to the radar system, the coherence loss is due to the different electrical path that different sub-band of the received signal experience. This is because the different sub-band shares only part of the internal circuitry. To compensate for such an effect the system includes a phase auto-calibration circuit. Such circuit requires first to acquire a full CW-SF scan in a controlled path, then the successive scans are calibrated using this data to correct phase misalignment. Moreover, the information acquired during the calibration process allows a complete equalization of the subsystems in terms of phase and amplitude. The calibration process is completely automated and repeated at regular intervals during measurements, allowing the effect of system thermal drift to be tracked and corrected.

After such an automatic internal calibration, the path through the cables and the

antennas still remains to be compensated for. To this end, measurements collected for a copper plate scatterer located at a known distance from the antennas are exploited. In particular, the plate distance is chosen so that the reflection coming from the copper plate is easily discernable from the antennas' mutual coupling. This allows us to estimate the *time-position* (after a Fourier transformation as data are in the frequency domain) of the plate, and hence, as the free-space path is known, the cable-antenna path length z_{ca} is determined. Therefore, the scattered field is approximated simply as

$$E_S(x_m, f) = S_{21} \exp(j4\pi f z_{ca}/c), \tag{2.1}$$

c being the speed of light in free-space.

2.3.1 2D experimental reconstructions in controlled environment

In this section only single slice reconstructions are shown.

The set up of the experiment is shown in Fig. 2.11. It refers to the case of two hollow metallic cylinders of $2m$ in height with circular cross sections of diameters $10cm$ and $6cm$, respectively, whose centers are located at a depth of $z = 40cm$ (with respect to the reference system reported in Fig. 1.1) that is at about $30cm$ from the second interface of the wall. Such scatterers are located behind a tuff wall of size $1\times1\times0.11m^3$ ($0.11m$ being the thickness). The dielectric permittivity and conductivity of the tuff wall are assumed known in the imaging algorithm. In particular, we set $\epsilon_b = 4\epsilon_0$ according to the outcome of the electromagnetic characterization procedure reported in [45]. The dispersive nature of the tuff as well as its losses are not considered in the

model.

The radar system is placed in front of the wall so that the antennas are at $10cm$ apart form the first wall interface. The measurements have been collected in the frequency band ranging from $800MHz$ to $3200MHz$ with a frequency step of 60MHz. Moreover, a synthetic aperture $\Sigma = [-0.5, 0.5]m$ has been synthesized where the scattered field is collected at a spatial step of $2.5cm$.

Finally, the scattering scene is located in a semi-anechoic environment where three sides of the room are covered with absorbing panels $2.5 \times 2.5m^2$ sized.

As to the imaging algorithm, an investigation domain $D_T = [-0.5, 05] \times [0.11, 1]m^2$ has been assumed and the TSVD truncation index N_T, in eq. 1.7, is chosen so as to retain the singular functions corresponding to the singular values not below $20dB$ of the maximum one. It is worth remarking that only half of the measurements are exploited in the imaging algorithm. That is, for imaging purposes, we retain only the measurements collected at a spatial step of $5cm$. Thus, the numerical procedure is computationally more effective and it is possible by resorting to the results concerning the degrees of freedom of the scattered field [33].

Differently to the previous synthetic cases, two different sets of data have been acquired in presence (total scattered field) and in absence of the scatterers (background field) so that the scattered field is obtained as their difference. The results concerning a two-dimensional slice taken at an height of about $0.35m$ are reported in Fig. 2.12. In particular, in panel [A] of such a figure the time-domain normalized amplitude of the scattered field is reported as a function of the receiving antenna's position (i.e., the so-called radargram) and obtained by Fourier transforming each single frequency domain trace. As can be seen, the visual inspection of such a figure makes a user

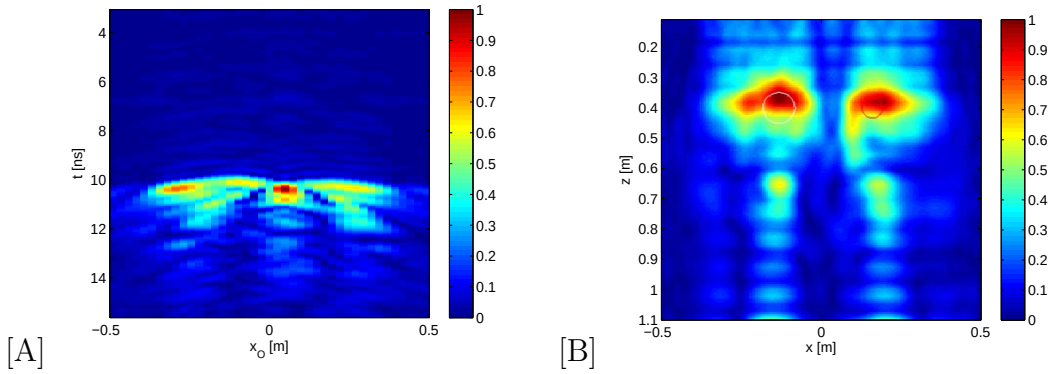

Figure 2.12: [A]: Radargram (non-calibrated normalized amplitude Fourier transformed data). [B]: Image obtained by the imaging algorithm. The actual scatterers' cross sections are also depicted as white and red circles.

aware only of the scatterer presence and little else. Note that the radargram has been obtained from non-calibrated data which only entails a shifting along the depth. Instead, the tomographic reconstruction reported in panel [B], obtained from calibrated data, is definitively better as the number and the locations of the scatterers can be clearly discerned (even though the antennas' behavior as well as the tuff dispersive law have been not accounted for in the model to achieve the inversions).

2.3.2 In situ 2D experiments

As a second example we go on to consider a more realistic scenario (see Fig. 2.13) in order to check the imaging algorithm in very realistic conditions. For such a case we placed the radar system so that the antennas are about $1cm$ away from the wall. In particular, an external bearing wall of the ground floor of one of the buildings of the faculty of engineering of the Second University of Naples has been chosen to perform the experiments. The scatterers to be imaged are located outside the building on the

Figure 2.13: Picture of the in situ scattering experiment.

opposite side of the wall (see panels [A] of Figs. 2.15 and 2.16).

The measurements have been collected in the frequency band ranging from $800MHz$ to $3200MHz$ with a frequency step of $1MHz$, over an aperture of $2m$ with a spatial step of $2cm$ and at an height of $0.74cm$ from the floor.

We know that the wall is made of tuff. Moreover, at the height measurements are taken, the wall is $24cm$ thick. Accordingly, in the imaging algorithm we adopted $\epsilon_w = 4\epsilon_0$ and $d = 24cm$. As in the previous case, the wall conductivity and dispersion law have not considered in the inversions.

As can be seen from Figs. 2.13 and 2.15 the scattering scenario is rather complex. The wall has a non-homogeneous thickness and above the place where the radar system is located there is a window. In this case it is also interesting to have a look at the radargram reported in Fig. 2.14 panel [A]. The radargram reveals the existence

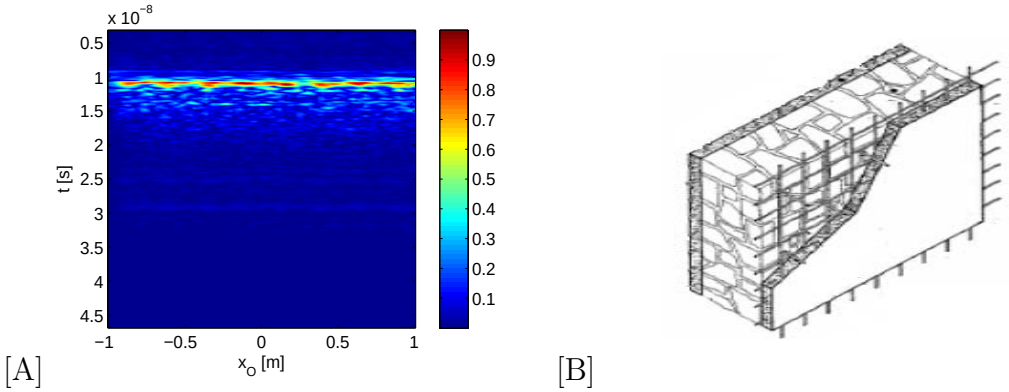

Figure 2.14: [A]: Radargram (non-calibrated normalized amplitude Fourier transformed data). [B]: Pictorial view of the reinforcing grid.

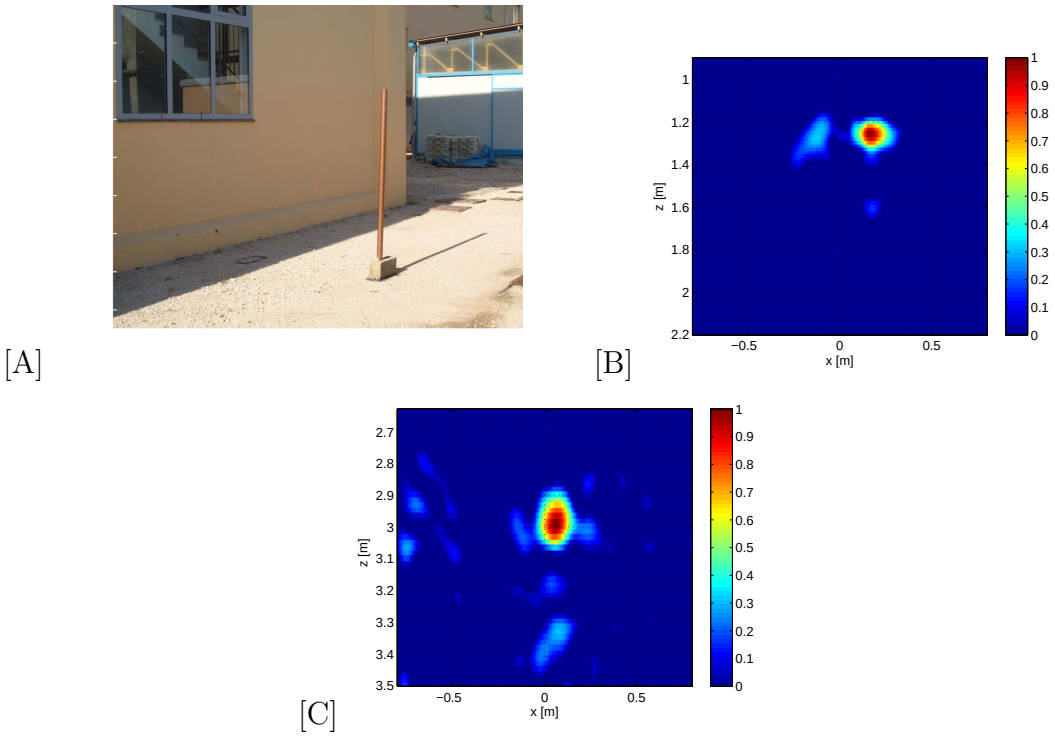

Figure 2.15: [A]: Picture of the scattering scene. [B]: Reconstruction of a metallic cylinder located at $1m$ beyond the wall. [C]: Reconstruction of a metallic cylinder located at about $2.6m$ beyond the wall.

of a periodic distribution of scatterers inside the wall which should be strong because the wall interfaces are not visible. The wall project confirmed that a steel reinforcing grid (see Fig. 2.14 panel [B] for a pictorial view of the grid) was present inside the wall.

However, we do not account for the reinforcing grid in the imaging algorithm still retaining the scattering model presented in Chapter 1. Moreover, the scattered field data are again obtained as the difference from the total field and the background one.

As in the previous case, while achieving the reconstruction we consider measurements taken at a double the spatial step (i.e., at $4cm$) used to obtain the radargrams. Furthermore, a measurement line $\Sigma = [-0.8, 0.8]m$, shorter than the one adopted for the radargram, is used. Finally, the data are also decimated in frequency. That is, we consider a frequency band $[1, 2.5]GHz$ sampled at a step of $75MHz$. This assures that waves penetrate through the grid and are not too affected by the attenuation introduced from the wall which is actually unknown.

Finally, in all the following reconstructions the TSVD has been truncated at the same level as done for the previous test-case.

The first in situ experiment concerns the case of a hollow metallic cylinder of circular cross section with a diameter of $6cm$ (see Fig. 2.15 panel [A]). In such a figure we consider two different situations. In panel [B], the cylinder center is located at $[0.18, 1.24]m$, that is at $1m$ beyond the wall, and an investigation domain $D = [-0.8, 0.8] \times [0.9, 2.2]m^2$. In panel [C], the cylinder is located at a greater distance from the wall $[0.03, 3]m$, that is at about $2.6m$ from the wall, and an investigation domain $D_T = [-0.8, 0.8] \times [2.65, 3.5]m^2$ is exploited in the imaging algorithm. As can be seen, in both cases the scatterer is detected and almost correctly localized despite

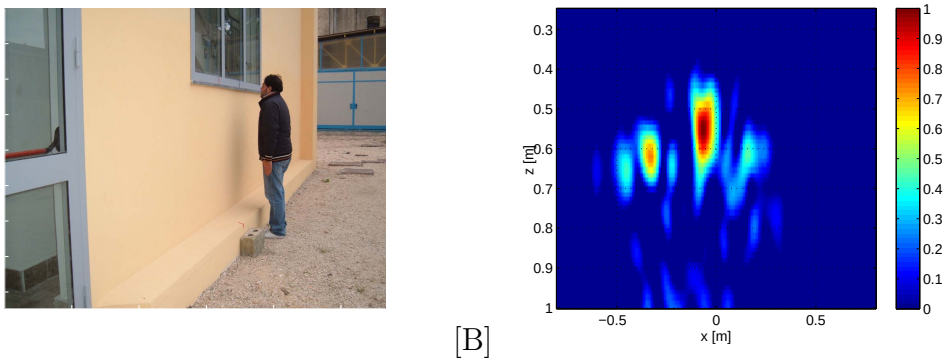

[A] [B]

Figure 2.16: [A]: Picture of the scattering scene in the case of human scatterers. [B]: Corresponding tomographic reconstruction.

all the assumption upon which the inversion scheme relies on.

As a final example we consider the case of a human being as scatterer (see Fig. 2.16 panel [A]). In particular, the center of such a scatterer is roughly located at $30cm$ from the wall and slightly shifted to the left with respect to the center of the measurement line.

According to the reference frame depicted in Fig. 1.1 the scatterer's location is about $[-0.1, 0.55]m$. For such an example we consider an investigation domain $D = [-0.8, 0.8] \times [0.25, 1]m^2$. The corresponding reconstruction reported in the same figure in panel [B] shows that the imaging algorithm works well in detecting and localizing this scatterer as well.

2.3.3 3D preliminary reconstructions

In this section we show some $3D$ experimental results obtained by exploiting measurements collected within an anechoic chamber at the Electromagnetic Diagnostics Laboratory of the Second University of Naples.

A reflection mode multi-bistatic/multifrequency configuration is exploited. Even though such a configuration is typical in TWI scenarios, the results we show refer to the case of non obscured scatterers. Therefore, they should be meant as preliminary to TWI applications. However, in order to stay within the framework of TWI applications, an anthropomorphic phantom is used as a scatterer and the possibility of taking measurements over a limited set of spatial points is considered. The latter is of particular interest because it affects the time required to collect data, particularly when the scanning is achieved through a moving system. It also impacts on the system complexity when a measurement array is employed.

In order to obtain $3D$ reconstructions data have to be acquired over a planar aperture. To this end, we adopted a different (with respect to the previous one) experimental set-up.

It consists of a positioning system and a measurement system which are remotely controlled and synchronized by a PC, thanks to a customized LabView software.

The positioning system is placed into a shielded anechoic chamber whose internal dimensions are $2.4m$ in depth, $3.4m$ in length and $2.6m$ in height.

The core of the measurement system is a Vectorial Network Analyzer (VNA), model Anritsu MS4624D $10MHz - 9GHz$, that has two internal sources and four ports connected to the passing technical panel of the anechoic chamber by means of $3m$ length coaxial cables.

The positioning system essentially consists of a double tower planar scanner: two vertical linear positioners ("towers") which can move independently over a horizontal linear positioner. This configuration allows, hence, the independent movement on a plane of two antennas. Absolute position is available by encoders placed along the

Figure 2.17: Picture of the planar scanner placed in the anechoic chamber

whole run of the four axes.

However, as mentioned above, here we adopted a multi-bistatic configuration. Hence, only a single tower of the positioning system, where the transmitting and the receiving antennas are mounted at a fixed distance along the horizontal axis, is employed to collect the measurements (see Fig. 2.17).

The maximum horizontal scanning length which can be achieved is $2.65m$, but a minimum distance of $25cm$ between the two towers is required. Hence, even if for the case at hand one of the towers is kept fixed the other tower (the one on which the antennas are mounted) can actually scan only a $2.40m$ horizontal segment. The maximum vertical run is $2.10m$.

The connection of the antennas to the exterior of the chamber is achieved by means of $8m$ length coaxial cables, screwed on coaxial connectors mounted on the

passing technical panel. The cables are mounted into a flexible guide in order to allow movement without excessive mechanically stress.

As far as the antennas are concerned, we use two wide band ridged horn antennas (Schwarzbeck Mess - Elektronik) suitably aligned so that they scan the same plane (see Fig. (2.17)and working in the band of $0.8 - 5.2GHz$. However, different kinds of antennas can be mounted on the system as well.

The measured parameter is the transmission coefficient S_{21} between the ports 1 and 2 of the VNA. Therefore, in order to make the measurements suitable for the inversion algorithm, as done before, first a standard "frequency transmission response" calibration is performed at the end of the cable chain, that is at the antenna input sections. Furthermore, as the inversion algorithm exploits the scattered field measurements, free-space measurements are needed. This way, the scattered field is obtained as the difference between the total field (i.e., the field measured in presence of the scattering objects) and the free-space measurements. This also allows to remove from the scattered field data the direct coupling between the antennas as the coupling effect can be considered constat over the two measurements.

Finally, we remark that in the following reconstruction examples and according to the previous section, we have assumed the antennas as being two-dimensional dipoles, that is the actual source plane-wave spectrum is not accounted for.

In all the following examples data are gathered over a measurement aperture $\Sigma = [0.35, 2.35]m \times [0.6, 2]m$ with the transmitting and the receiving antennas separated by a $\Delta_x = 30cm$ (measured from the two aperture centers). The investigation domain is $D = [0.35, 2.35] \times [0.6, 2]m \times [1, 1.7]m$ (the quota along z is measured from the antenna aperture). As we have in mind TWI applications, the frequency band is chosen as in

Figure 2.18: Picture of the mannequin within the anechoic chamber.

the previous example, that is $[0.8, 3.2]GHz$, for which most of the building materials are relatively transparent [10]. Moreover, a plastic mannequin $1.80m$ in height covered by aluminium foil is considered as a scatterer to be reconstructed. In particular, the mannequin has been placed over a dielectric pedestal $10cm$ in height so that it covers the investigation domain in height from $y = 0.6m$ to $1.9m$ (see Fig. 2.18). Finally, in the following reconstructions the modulus of the regularized retrieved unknown, $|\mathcal{R}\gamma|$, is obtained by retaining in the TSVD expansion the singular functions corresponding to the singular values not below $-20dB$ (this truncation roughly corresponds to the beginning of abrupt decay of the singular values).

The experiment results are shown in Figs. 2.19 and 2.20. They refer to the case where the mannequin center is roughly located at $x = 1.95m$ and $z = 1.45m$. For such a case, 21 equally spaced slices have been considered and for each slice the measurement line has been uniformly sampled at a step of $4cm$ so that 51 measurements are taken. Moreover, 11 uniformly spaced frequencies, within the band reported above, have been used. Fig. 2.19 shows the different slice reconstructions for which can be appreciated that the scatterer is detected and correctly localized. After obtaining the $2D$ slices, they are first normalized to the "global" maximum (i.e., the maximum over each slices) and then thresholded as described in [23]. Finally, an isosurface representation is adopted to display the $3D$ reconstruction (see Fig. 2.20). As can be seen, from the $3D$ representation (frontal view) the phantom is very well localized (as obvious from the slices) and its silhouette roughly retrieved; hence, it greatly improve the understanding about the scatterer.

A critical point towards the speeding of the imaging procedure (i.e., the data collection plus the image formation) is the number of data to be used. Indeed, the number of necessary data affects both the time required for data collection and the time required for the TSVD image computation. Moreover, it also enters in the necessary memory storage.

To cope with this question the evaluation of the so-called number of degrees of freedom (NDF) plays a central role [46].

Therefore, in order to make the imaging computationally more effective results concerning the NDF reported in [47] have been resorted to. In particular, for the measurement configuration exploited above, it is found that at the highest adopted frequency 26 measurement points (for each slice) could be enough (this number has

been maintained also for the lower frequencies). As to the frequencies, we still adopt 11 frequencies, which are slightly beyond the optimal number derived in [38], because time required for frequency sweep is negligible with respect to that required for spatial scanning. The reconstruction of the same scatterer as in Figs. 2.19 and 2.20 by employing the new measurement parameters is reported in Fig. 2.21.

As can be seen, the quality of the reconstruction is practically the same as the one previously reported. This is also a remarkable result if one looks at other imaging methods present in the literature which have shown to work for a finer data collection grid [9, 20].

In view of the reduced number of data the imaging algorithm takes few seconds to achieve the images. Instead, the time to acquire the data is still a critical figure for sliding systems as the one at hand. However, if the measurements were taken quasi-instantaneously, for example by employing an antenna array, changes during data acquirement can be neglected (so image focusing degradation is avoided) and the simple change detection procedure, previously presented, can be employed to counteract the clutter due to static scatterers.

Experimental results concerning the change detection procedure are shown in the next section.

2.3.4 Testing the change detection procedure by experimental data

In this section we turn to show some examples, for $2D$ as well as $3D$ cases, concerning the change detection procedure obtained by experimental data. More in detail, the $2D$ examples have been obtained for the scattering scenario and the radar system

already considered in section 2.3.2, whereas the $3D$ examples refer to the scattering scenario and the radar system adopted in section 2.3.3.

Accordingly, the $2D$ examples have been obtained for a realistic scenario with the radar system located very close to an external wall of the ground floor of one of the buildings of the faculty of engineering of the Second University of Naples. As explained in section 2.3.2, for such a case, the wall has thickness equal to $0.24m$ and dielectric permittivity of $4\epsilon_0$. The target to be imaged is a metallic circular cylinder having radius of $0.03m$ located outside the building on the opposite side of the wall (see Fig. 2.22 for a pictorial view of the scene). The data are collected along a line at $0.74m$ from the floor and the same configuration parameters as reported in TAB. 2.1 are adopted except for the frequency step, which is now of $25MHz$, and for the investigation domain which is $D = [-0.8, 0.8] \times [0.7, 3.5]m^2$.

We consider only two configurations:

$m = 1$, the target center is at about $(0.17, 1.2)m$

$m = 2$, the target center is at about $(0.3, 3)m$.

No further scatterers are present within the investigation domain so that the clutter arises from errors in modeling the wall. In particular, to emphasize this point, the reconstructions are obtained by adopting the total scattered field (i.e., the field reflected by the wall plus the one scattered by the target behind it).

The reconstructions corresponding to the two cases mentioned above are reported in panels $[A]$ and $[C]$ of Fig. 2.22. As can be seen, they look very similar and no information about the scatterers can be deduced. More in detail, as we known the wall parameters, a part from the wall contribution which would be manifested as two line due to the two interfaces, we expected the target being localized [10]. Indeed, in

both cases the target is very hard to be detected. This is due to a steel reinforcing grid present within the wall we completely neglected in the model and which obscures the scatterers located beyond it. Amazingly, the change detection procedure dramatically increases the detectability of the scatterers (see panels $[B]$ and $[D]$) even though some spurious artifacts still remain for the more deeply located scatterer.

We now switch to consider a $3D$ example. As mentioned above, to this end, we refer to the preliminary free-space configuration addressed in section 2.3.3.

For such a case, in order to verify experimentally the principle of the method proposed in [27] we turn to consider two different situations in which the mannequin is located at two different positions whereas a static scatter is present in the scene at the same position [30]. The reconstructions corresponding to these two cases are reported in Fig. 2.23: both the scatterers are well localized even though in the case 2 the scatterer on the left has a worse reconstruction. This is because in the case 2, the mannequin is more strongly (in amplitude) reconstructed being located in the middle of the scene. Therefore, while applying the threshold (which is set up according to the maximum of the overall reconstruction) some parts of the reconstruction of the scatterer on the left are discarded as well. Anyway, in general, it is not easy to discern the human being scatterer.

As described above, the presence of a moving scatterer can be evidenced if the reconstruction at a given instant of time is obtained by subtracting, pixel by pixel, such a reconstruction and a reconstruction obtained in a previous (or even subsequent) instant of time. For the cases at hand, this means that

$$|\mathcal{R}\gamma_2| - |\mathcal{R}\gamma_1| \tag{2.2}$$

and

$$|\mathcal{R}\gamma_1| - |\mathcal{R}\gamma_2|, \tag{2.3}$$

where $|\mathcal{R}\gamma_1|$ and $|\mathcal{R}\gamma_1|$ are the reconstruction reported in panel [A] and [B] of Fig. 2.23, respectively, and $|\mathcal{R}\gamma_2| - |\mathcal{R}\gamma_1|$ and $|\mathcal{R}\gamma_1| - |\mathcal{R}\gamma_2|$ are the difference images which actually are employed to localized the moving scatterer in the case 1 and 2. The result of this procedure is reported in Fig. 2.24. As can be seen, the procedure works very well and the results are quit remarkable if one thinks that it did not required a reference background image as is the case of other difference image procedure.

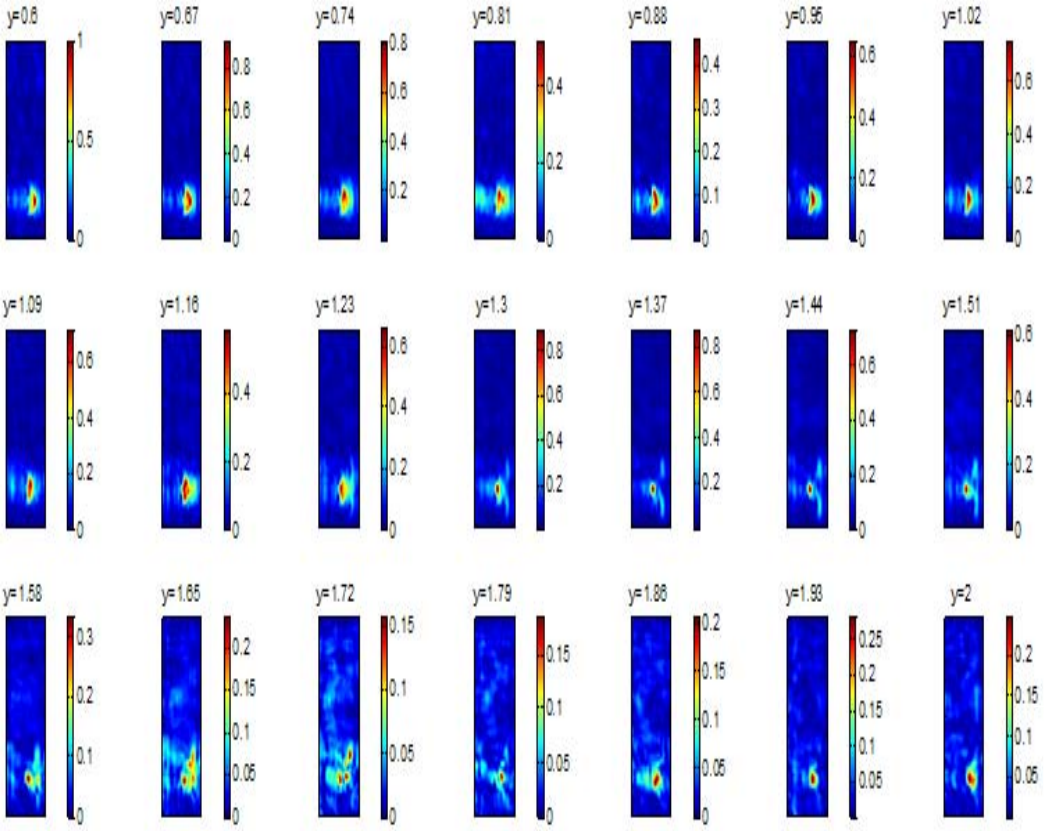

Figure 2.19: Slice reconstructions of the mannequin.

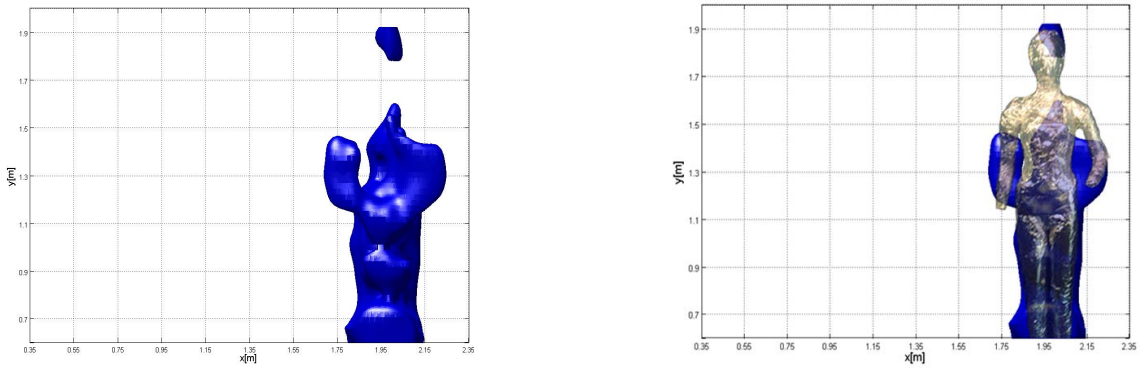

[A] [B]

Figure 2.20: Frontal view (looking at along the z-axis) of the 3D reconstruction obtained by interpolating the 2D slices. The panel [A] reports the reconstruction only, whereas the panel [B] shows the reconstruction and the mannequin at its actual position.

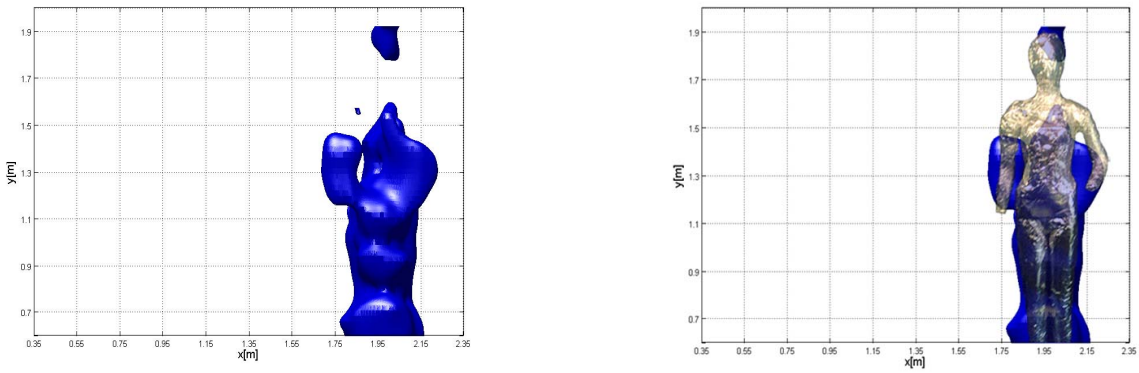

[A] [B]

Figure 2.21: Frontal view (looking at along the z-axis) of the 3D reconstruction obtained by collecting data according to the NDF. The panel [A] reports the reconstruction only, whereas the panel [B] shows the reconstruction and the mannequin at its actual position.

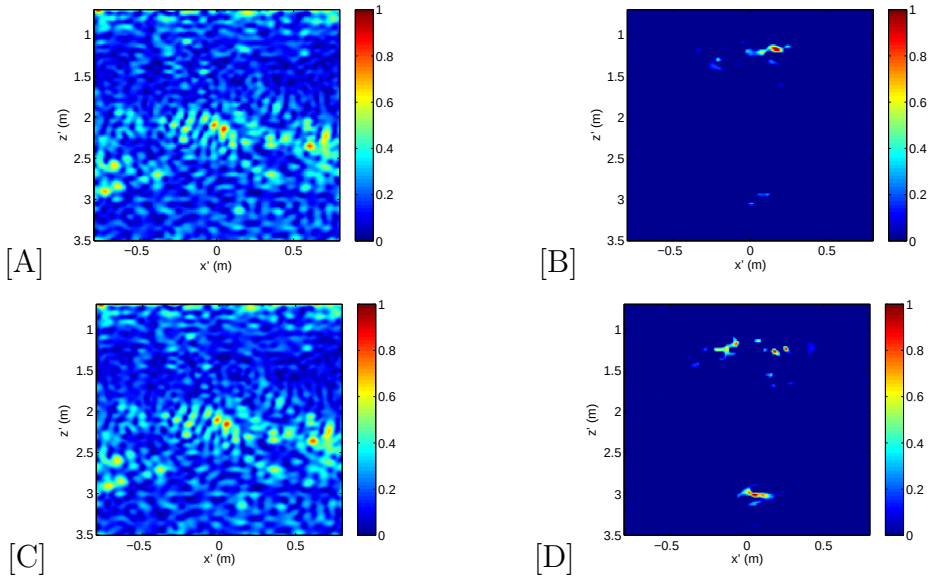

Figure 2.22: Normalized TSVD tomographic reconstructions and outcomes of the change detection procedure. [A]: $|\mathcal{R}\gamma_1|$ [B]: $|\mathcal{R}\gamma_1| - |\mathcal{R}\gamma_2|$. [C]: $|\mathcal{R}\gamma_2|$. [D]: $|\mathcal{R}\gamma_2| - |\mathcal{R}\gamma_1|$.

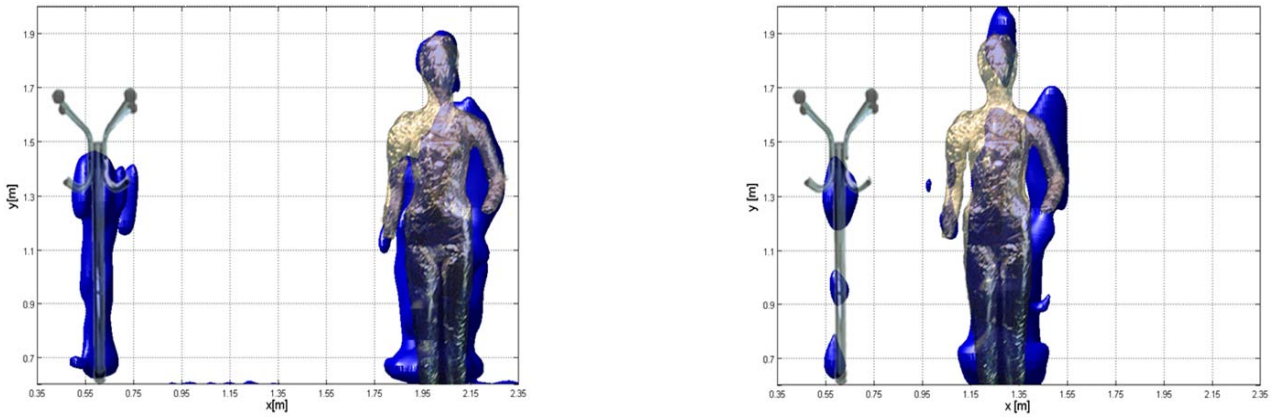

[A] [B]

Figure 2.23: 3D reconstructions for two different scatterers layout. The reconstructions and the actual scatterers are both reported. The parameters of the configuration are the same as in Fig. 2.21. The panel [A] is referred as the case 1 and the panel [B] as the case 2.

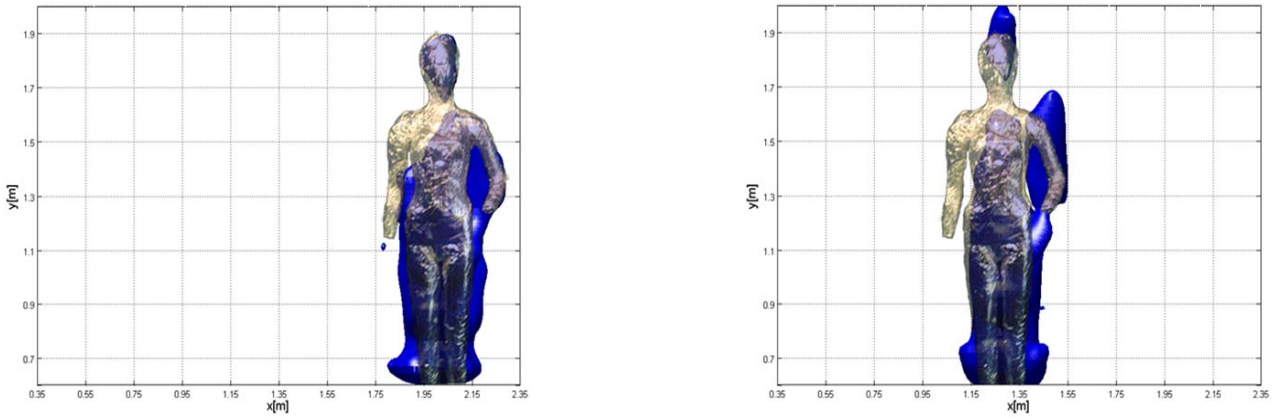

[A] [B]

Figure 2.24: Difference 3D reconstructions. The reconstructions and the actual scatterers are both reported. The parameters of the configuration are the same as in Fig. 2.21. The panel [A] reports $|\mathcal{R}\gamma_2| - |\mathcal{R}\gamma_1|$ whereas the panel [B] reports $|\mathcal{R}\gamma_1| - |\mathcal{R}\gamma_2|$.

Chapter 3

Conclusions

The problem of imaging scattering objects that are hidden by an obstacle layer has been addressed under ambiguous wall parameters. To tackle such a problem we have developed a novel two step based reconstruction procedure.

In the first step the wall parameters are estimated as the ones corresponding to the minimum of the cost functional reported in eq. (1.13). In particular, such a cost functional has been devised to minimize the effect of the field scattered by the obscured objects on the reliability of the estimation procedure.

The proposed approach overcomes the limits of the methods presented in [15, 16, 17] which rely on the scattered field. Indeed, when the wall is unknown it is difficult to extract the scattered field from the total scattered field which accounts for the strong clutter arising from the wall itself. Differently, the developed estimation procedure exploits the total scattered field and allows to solve the problem of wall clutter mitigation. In fact, once the wall parameters are determined the field scattered by the hidden objects can be retrieved by subtracting from the total field an estimated version of the field reflected by the wall. Moreover, the presented estimation procedure can be considered a generalized more stable (against uncertainties and noise) version

of the method presented in [10] where measurements collected at a single position are exploited.

Numerical examples testify that the proposed estimation procedure is fast, reliable and robust against noise also for the realistic situation of a finite wall structure.

Afterwards, having estimated the wall parameters, the reconstructions have been obtained by a tomographic imaging algorithm based on the Kirchhoff approximation and on the TSVD inversion scheme. As outlined, this method allows us to exactly account for the propagation through the wall and results in a better mitigation of the image blurring due to the obstacle.

Two-dimensional and a three-dimensional synthetic reconstructions have been presented. In particular, the three-dimensional reconstruction has been obtained by the sliced approach presented in [23] for the case of a strong scatterer miming the human body.

The inversion algorithm has been tested by exploiting synthetic data and has proved capable of detecting and localizing the objects' "silhouette" for relatively low SNR.

However, to assess the performances that an imaging algorithm can actually achieve it is mandatory to validate it against experimental data, in particular for realistic scenarios. To this end, we have checked the imaging algorithm against experimental data collected both in a controlled environment and on in situ experiments. It is shown that the proposed imaging algorithm is able to detect and localize the scatterers even in complex scattering scenarios whose features are not completely accounted for by the adopted model. In particular, for the $3D$ cases, we have considered

objects resembling the human body. However, even though the measurement parameters have been chosen with TWI applications in mind, the experiments have been preliminary conducted for a free space situation and within a controlled environment.

Despite the simplicity of the inversion algorithm, the analysis has shown that it allows to localize and to roughly determine the shape of the scatterers dealing with large (in terms of the wavelength) investigation domains. Moreover, by selecting the measurement points and the frequencies according to the degrees of freedom of the scattered field, the reconstruction algorithm becomes very quickly. This open the way to the possibility to detect moving targets in order to discern human being from static background clutter.

In this regard, a simple procedure based on the incoherent difference between two reconstructions (not requiring a reference background image) to detect change in the imaging scenario has been presented and validated both in synthetic and experimental data.

Of course, the results presented herein have to be meant as a proof of the principle. Indeed, we have used a sliding system to synthesize the measurement aperture which requires a non negligible time to acquire the data, even though data are collected according to the the NDF. Antenna arrays would be a more suitable choice to make the change detection technique useful for practical real time moving target tracking.

As further developments we identify the need to relax the assumptions concerning the nature of the wall structure in order to deal with a more complex background environment. This has been done, for example in [43], where a background resembling the room of a building has been considered. In that case, it was shown that it is sufficient to account for the wall over which the measurement array is synthesized to

avoid distortions in the reconstructions.

However, in [43], as here, the wall structure has been assumed homogeneous. In many realistic situations such a hypothesis does not hold. Therefore, further efforts have to be done to deal with more complex scenarios also in view of the fact that such cases require an increased number of parameters in the wall description which could affect the reliability and the effectiveness of the optimization stage upon which the estimation procedure is based. In particular, we are now working to the case of layered wall where the number of layers as well as their electromagnetic features are unknown.

Further developments concern the need to account for more realistic sources by means of their radiation patterns in the estimation as well as in the imaging procedures [48].

Finally, experimental validation for a three-dimensional in situ scene is needed to assess the actual performances achievable by the estimation/reconstruction procedure.

Bibliography

[1] A. R. Hunt, Image Formation Through Walls Using a Distributed Radar Sensor Array", Proceedings of the 32nd Applied Imagery Pattern Recognition Workshop (AIPR'03) IEEE, 2003.

[2] A. M. Attiya, A. Bayram, A Safaai-Jazi, and S. M. Riad,"UWB Applications for Through-Wall Detection," IEEE Antennas and Propagation Society International Symposium, pp. 3079-3082, 2004.

[3] F. Aryanfar, and K. Sarabandi, "Through Wall Imaging at Microwave Frequencies Using Space-Time Focusing," IEEE Antennas and Propagation Society International Symposium, pp. 3063-3066, 2004.

[4] D.D. Ferris, and N.C. Currie, "A Survey of Current Technologies for Through-Wall-Surveillance (TWS)", Proceedings of SPIE, vol. 3577, pp. 62-72, 1998.

[5] F. Soldovieri, R. Solimene, A. Brancaccio, and R. Pierri, " Localization of the Interfaces of a Slab Hidden Behind a Wall," *IEEE Trans. Geosci. Remot. Sens.*, vol. 45, pp. 2471-2482, 2007.

[6] L. Frazier, "MDR for Law Enforcement," *IEEE Potentials*, vol. 16, pp. 23-26, 1998.

[7] Y. Yang, and A. E. Fathy, "See-Through-Wall Imaging Using Ultra Wideband Short-Pulse Radar System," IEEE Antennas and Propagation Society International Symposium, pp. 334-337, 2005.

[8] M. Farwell, J. Ross, R. Luttrell, D. Cohen, W. Chin, T. Dogaru, "Sense Through the Wall System Development and Design Considerations, Journal of Franklin Institute, Special Issue on Advances in Indoor Radar Imaging, vol. 345, pp. 570-591, 2008.

[9] F. Ahmad, M. G. Amin, S. A. Kassam, "Syntethic Aperture Beamformer for Imaging Through a Dielectric Wall," *IEEE Trans. Aerosp. Electr. Systm.*, vol. 41, pp. 271-283, 2005.

[10] M. Dehmollaian, K. Sarabandi, "Refocusing Through Building Walls Using Synthetic Aperture Radar," *IEEE Trans. Geosc. Rem. Sens.*, vol. 46, pp. 1589-1599, 2008.

[11] F. Soldovieri, R. Solimene, "Through-Wall Imaging Via a Linear Inverse Scattering Algorithm," *IEEE Geosc. Rem. Sens. Lett.*, vol. 4, pp. 513-517, 2007.

[12] L.P. Song, C. Yu, and Q.H. Liu, "Through-Wall Imaging (TWI) by Radar: 2-D Tomographic Results and Analyses," *IEEE Trans. Geosci. Remot. Sens.*, vol. 43, pp. 2793-2798, 2005.

[13] R. Pierri, A. Liseno, R. Solimene, F. Soldovieri, "Beyond Physical Optics SVD Shape Reconstruction of Metallic Cylinders," *IEEE Trans. Antennas Propag.*, vol. 54, pp. 655-665, 2006.

[14] M. Bertero and P. Boccacci, *Introduction to Inverse Problems in Imaging* (Institute of Physics, Bristol, UK 1998).

[15] G. Wang, M. G. Amin, Y. Zhang, "New Approach for Target Locations in the Presence of Wall Ambiguities," *IEEE Trans. Aerosp. Electr. Systm.*, vol. 42, pp. 301-315, 2006.

[16] G. Wang, M G. Amin, "Imaging Through Unknown Walls Using Different Standoff Distances," *IEEE Trans. Sing. Process.*, vol. 54, pp. 4015-4025, 2006.

[17] F. Ahmad, M. G. Amin, G. Mandapati, "Autofocusing of Through-The-Wall Radar Imagery Under Unknown Wall Characterisitics," *IEEE Trans. Imag. Process.*, vol. 16, pp. 1785-1795, 2007.

[18] E. J. Rothwell, K. M. Chen, D. P. Nyquist, W. Sun, "Frequency Domain E-pulse Synthesis and Target Discrimination," *IEEE Trans. Antenn. Propag.*, vol. 35, pp. 426-434, 1987.

[19] G. J. Stenholm, E. J. Rothwell, D. P. Nyquist, L. C. Kempel, L. L. Frasch, "E-pulse Diagnostics of Simple Layered Materials," *IEEE Trans. Antenn. Propag.*, vol. 51, pp. 3221-3227, 2003.

[20] M. Dehmollaian, M. Thiel, and K. Sarabandi, "Through-the-Wall Imaging Using Differential SAR," *IEEE Trans. Geosc. Rem. Sens.*, vol. 47, pp. 1289-1296, 2009.

[21] R. Solimene, F. Soldovieri, G. Prisco, R. Pierri,"Three-Dimensional Through-Wall Imaging Under Ambigous Wall Parameters," *IEEE Trans. Geosc. Rem. Sens.*, vol. 47, pp. 1310-1317, 2009.

[22] F. F. Ahmad, Y. Y. Zhang, M. G. Amin, "Three-Dimensional Wideband Beamforming for Imaging Through a Single Wall," *IEEE Geosc. Rem. Sens. Lett.*, vol. 5, pp. 176-179, 2008.

[23] R. Solimene, F. Soldovieri, G. Prisco, R. Pierri, "3D Microwave Tomography by a 2D Slice Based Reconstruction Algorithm," *IEEE Geosc. Rem. Sens. Lett.*, vol. 4, pp. 556-560, 2007.

[24] S. Y. Semenov, R. H. Svenson, A. E. Boulyshev, A. E. Souvorov, V. Y. Borisov, Y. Sizov, A. N. Starostin, K. R. Dezern, G. T. Tatsis, and V. Y. Baranov, "Microwave Tomography: Two-Dimensional System for Biological Imaging," *IEEE Transactions on Biomedical Engineering*, vol. 43, pp. 869-876, 1996.

[25] Y. Yang, and A. E. Fathy, "Development and Implementation of a Real-Time See-Through-Wall Radar System Based on FPGA," *IEEE Trans. Geosc. Rem. Sens.*, vol. 47, pp. 1270-1280, 2009.

[26] Moulton, J., S. Kassam, F. Ahmad, M. Amin, and K. Yemelyanov, "Target and Change Detection in Synthetic Aperture Radar Sensing of Urban Structures, Proceedings of the IEEE Radar Conference (RADAR08), 2008.

[27] F. Soldovieri, R. Solimene, R. Pierri, "A Simple Strategy to Detect Changes in Through the WAll Imaging," *Progress In Electromagnetics Research M*, vol. 7, pp. 1-13, 2009.

[28] F. Soldovieri, R. Solimene, A. Brancaccio, and R. Pierri, "TWI Experimental Results by a Linear Inverse Scattering Approach," *Progress In Electromagnetics Research*, vol. PIER 91, pp. 259-272, 2009.

[29] F. Soldovieri, R. Solimene, A. Brancaccio, and R. Pierri, "First Experimental Results for a Linear Inverse Scattering TWI Approach," Proceedings of the European Microwave Week 2009 , Roma, Italy.

[30] R. Solimene, A. Brancaccio, R. Di Napoli, and R. Pierri, "3D Sliced Tomographic Inverse Scattering Experimental Results," submitted.

[31] W. C. Chew, *Waves and Fields in Inhomogeneous Media* (IEEE Press, Piscataway, NJ, 1995).

[32] P. C. Hansen, J. G. Nagy, D. P. OLeary, *Deblurring Images: Matrices, Spectra, and Filtering* (SIAM, 2008).

[33] R. P. Porter and A. J. Devaney, "Generalized Holography and Computational Solutions to Inverse Source Problems, *J. Opt. Soc. Am. A* vol. 72, pp. 1707-1713, 1982.

[34] N. Levanon, *Radar Principles* (Wiley, New York, 1988).

[35] D. Potin, E. Duflos, and P. Vanheeghe, "Landamines Ground Penetrating Radar Signal Enhancement by Digital Filtering, *IEEE Trans. Geosc. Rem. Sens.*, vol. 44, pp. 23932406, 2006.

[36] J. Li, and E. G. Zelnio, "Target Detection with Synthetic Aperture Radar, *IEEE Trans. Aerosp. Electr. Syst.*, vol. 32, pp. 613627, 1996.

[37] M. Maaref, P. Millot, C. Pichot, and O. Picon, "A Study of UWB FM-CW Radar for the Detection of Human Beoings in Motion Inside a Building," *IEEE Trans. Geosc. Rem. Sens.*, vol. 47, pp. 1297-1300, 2009.

[38] R. Persico, F. Soldovieri, G. Leone, "A Microwave Tomographic Imaging Approach for Multibistatic Configuration: the Choice of the Frequency Step," *IEEE Trans. Instrum. Meas.*, vol. 55, pp. 1926-1934, 2006.

[39] A. F. Peterson, S. L. Ray, R. Mittra, *Computational Methods for Electromagnetics* (IEEE Press, NJ, 1998).

[40] D. J. Daniels, *Ground Penetrating Radar*, 2nd Edition, IEE Radar, Sonar, Navigation and Avionics series, (IEE Press, London, UK, 2004).

[41] http://www.ansoft.com/products/hf/hfss/

[42] A. Giannopoulos, "GprMax2D/3D, Users Guide," www.gprmax.org, 2002.

[43] F. Soldovieri, R. Solimene, G. Prisco, "A Multiarray Tomographic Approach for Through-Wall Imaging," *IEEE Trans. Geosci. Remot. Sens.*, vol. 46, pp. 1192-1199, 2008.

[44] F. Parrini, M. Fratini, M. Pieraccini, C. Atzeni, G. De Pasquale, P. Ruggiero, F. Soldovieri and A. Brancaccio, "ULTRA: Wideband Ground Penetrating Radar," Proc. of European Radar Conference EURAD2006, Manchester, UK, Sept. 2006.

[45] A. Brancaccio, F. Soldovieri, G. Leone, D. Sglavo and R. Pierri, "Microwave Characterization of Materials in Civil Engineering," *Proc. European Microwave Assoc.*, vol. 6, pp. 128-135, 2006.

[46] R. Solimene, and R. Pierri, "Number of Degrees of Freedom of the Radiated Field Over Multiple Bounded Domains," *Opt. Lett.*, vol. 32, NO. 21, pp. 3113-3115, 2007.

[47] A. Brancaccio, G. Leone, R. Pierri, "Information content of Born scattered fields: results in the circular cylindrical case, *J.Opt. Soc. Am. A* vol. 15, pp. 1909-1917, 1998.

[48] F. Soldovieri, G. Prisco, R. Solimene, "Equalization of the Antenna Pattern in Shape Reconstrucion of Metallic Objects," *IEEE Trans. Ant. Prop.*, vol. 54, pp. 3865-3873, 2006.

List of Symbols

Table 3.1: List of Symbols.

Symbol	Meaning	Where it appears for the first time
d	wall thickness	pp. 7
ϵ_b	dielectric permittivity of the wall	pp. 7
ϵ_0	free-space dielectric permittivity	pp. 7
μ_0	free-space magnetic permeability	pp. 7
D	investigation domain	pp. 8
Σ	observation domain	pp. 8
$\underline{E}_i(\cdot)$	field incident on the wall	pp. 9
$\hat{\underline{E}}_i(\cdot)$	incident field plane-wave spectrum	pp. 9
$\hat{i}_y$	unitary vector along y	pp. 9
k_0	free-space wavenumber	pp. 9
$[k_{0min}, k_{0max}]$	wavenumber band	pp. 9
$\underline{r} = (x, z)$	field point for a 2D geometry	pp. 9
$\underline{r}_S = (x_S, z_S)$	source point for a 2D geometry	pp. 9
u	spectral variable	pp. 9
$\underline{y}$	heights' vector	pp. 9
$E_S^0(\cdot)$	field scattered by the obscured scatterers	pp. 9
$E_t(\cdot)$	field transmitted trough the wall and impinging on the scatterers	pp. 9
$G(\cdot)$	three-layered background Green's function	pp. 9
D_T	investigation domain cross section	pp. 9
$\gamma(\cdot)$	unknown shape function	pp. 9

Symbol	Meaning	Where it appears for the first time
$n(\cdot)$	vector normal to the scatterers'contours	pp. 9
x_m	measurement point along a line at a fixed height	pp. 9
$U(\cdot)$	Heaviside function accounting for the scatterers'lit sides	pp. 10
δ_C	distribution defined over the scatterers'contours	pp. 10
$\hat{i}_z$	unitary vector along z	pp. 10
$\tau(\cdot)$	wall transmission coefficient	pp. 10
Γ_{0b}	air/obstacle local reflection coefficient	pp. 10
z_1	depth of the wall first interface	pp. 11
$\mathcal{R}\gamma(\cdot)$	regularized reconstruction	pp. 11
$\{u_n, \sigma_n, v_n\}_{n=0}^{\infty}$	scattering operator singular system	pp. 11
N_T	SVD truncation index	pp. 11
$E_S(\cdot)$	total scattered field	pp. 13
$E_S^w(\cdot)$	field reflected by the wall	pp. 13
$(\hat{\epsilon}_d, \hat{d})$	estimated wall parameters	pp. 13
$\Gamma(\cdot)$	wall reflection coefficient	pp. 13
$P_{[0,T_e]}$	time limiting projector over $[0, T_e]$	pp. 13
T_e	time interval used in the estimation process	pp. 13
Ω	frequency band	pp. 13
$\mathcal{F}_\Omega$	Fourier transform operator over Ω	pp. 13
$\tilde{d}$	distance function	pp. 13
E_{sav}	averaged total scattered field	pp. 13
c	speed of light in free-space	pp. 14
$E_{SC}(\cdot)$	field scattererd by static obscured scatterers	pp. 16
$E_{ST}(\cdot)$	field scattered by moving obscured scatterers	pp. 16
m	vector indexing different time data collections	pp. 17
N	size of m	pp. 17
ϵ	human phantom dielectric permittivity	pp. 24
σ	human phantom conductivity	pp. 24
S_{21}	measured scattering paramenter	pp. 34
z_{ca}	cable-antennas path	pp. 35

List of Abbreviations and Acronyms

Table 3.2: List of Acronyms.

Acronym	Meaning	Where it appears for the first time
TWI	Through-Wall-Imaging	pp. x
TSVD	Truncated Singular Value Decompositioni	pp. xi
NDF	Number of degrees of freedom	pp. 11
GPR	Ground Penetrating Radar	pp. 16
MTI	Moving Target Indicator	pp. 16
SNR	Signal to Noise Ratio	pp. 20
MOM	Method of Moments	pp. 21
EFIE	Electric Field Integral Equation	pp. 21
HFSS	High Frequency Structural Simulator	pp. 19
FEM	Finite Element Method	pp. 24
FDTD	Finite Difference Time Domain	pp. 27
USB	Universal Serial Bus	pp. 32
CW-SF	Continuous Wave-Stepped Frequency	pp. 34
VNA	Vector Network Analyzer	pp. 42